Tectonics

RESEARCH ARTICLE
10.1029/2020TC006242

Key Points:
- Three deformation events record prograde-to-peak metamorphism (D1), exhumation from eclogite-facies conditions (D2), and postcollisional folding (D3)
- White mica $^{40}Ar/^{39}Ar$ dates evince both closure of ^{40}Ar diffusion and subsequent partial resetting due to deformation during Scandian thrusting
- Exhumation of the Tsäkkok Lens from eclogite-facies to midcrustal/shallow-crustal conditions was rapid (<10 Myr)

Supporting Information:
- Supporting Information S1
- Table S1
- Table S2

Correspondence to:
C. J. Barnes,
cjbarnes063@gmail.com

Citation:
Barnes, C. J., Jeanneret, P., Kullerud, K., Majka, J., Schneider, D. A., Bukała, M., & Klonowska, I. (2020). Exhumation of the high-pressure Tsäkkok Lens, Swedish Caledonides: Insights from the structural and white mica $^{40}Ar/^{39}Ar$ geochronological record. *Tectonics*, *39*, e2020TC006242. https://doi.org/10.1029/2020TC006242

Received 11 APR 2020
Accepted 19 MAY 2020
Accepted article online 12 JUN 2020

Exhumation of the High-Pressure Tsäkkok Lens, Swedish Caledonides: Insights From the Structural and White Mica $^{40}Ar/^{39}Ar$ Geochronological Record

C. J. Barnes[1], P. Jeanneret[2,3], K. Kullerud[4,5], J. Majka[1,2], D. A. Schneider[6], M. Bukała[1], and I. Klonowska[1]

[1]Faculty of Geology, Geophysics and Environmental Protection, AGH University of Science and Technology, Krakow, Poland, [2]Department of Earth Sciences, Uppsala University, Uppsala, Sweden, [3]Laboratoire Chrono-environnement, Université de Bourgogne Franche-Comté, Besançon, France, [4]Department of Geology, University of Tromsø, Tromsø, Norway, [5]Norwegian Mining Museum, Kongsberg, Norway, [6]Department of Earth and Environmental Sciences, University of Ottawa, Ottawa, Ontario, Canada

Abstract Integrated structural, geochemical, and geochronological investigations were conducted on metasedimentary rocks in the eclogite-bearing Tsäkkok Lens of the Seve Nappe Complex (Scandinavian Caledonides) to resolve its exhumation history. Three deformation events are defined. D1 is likely related to the prograde to peak-metamorphic stages, represented by a locally preserved S1. D2 resulted in vertical shortening and is defined by a pervasive S2 and cm-/m-scale F2 closed folds. D2 terminated with Scandian thrusting, which emplaced the overlying Köli Nappe Complex. D3 records NE-SW shortening and constitutes m-/km-scale F3 open folds that deformed the Tsäkkok Lens and Köli Nappe Complex together. In situ white mica $^{40}Ar/^{39}Ar$ geochronology was conducted on select metasedimentary samples possessing S1 or S2 to resolve the timing of exhumation. Postdecompression cooling of the Tsäkkok Lens is best recorded by samples containing S1 or S2 that yield homogeneous white mica chemistry and $^{40}Ar/^{39}Ar$ dates. The timing of cooling is resolved to 477.2 ± 4.1 Ma (S1) and 475.3 ± 3.5 Ma (S2). Vertical shortening of the lens during exhumation may have proceeded until 458.1 ± 9.0 Ma. Later-stage deformation during Scandian thrusting penetrated the Tsäkkok Lens at 429.9 ± 9.0 Ma, or younger. This resulted in noncoaxial deformation of the metasedimentary rocks, producing heterogeneous white mica chemistry and partially reset the older $^{40}Ar/^{39}Ar$ cooling record. Temperatures for deformation are resolved to the upper greenschist-lower amphibolite facies. Altogether, the Tsäkkok Lens records rapid exhumation from eclogite-facies conditions to midcrustal depths or shallower, followed by emplacement of the overlying Köli Nappe Complex.

1. Introduction

Since the discovery of continental crust subduction to ultrahigh pressure (UHP) conditions (e.g., Chopin, 1984; Smith, 1984), the mechanisms for exhumation of the subducted crust have been the subject of significant discussion (e.g., Andersen et al., 1991; Chemenda et al., 1995; Chopin, 2003; Ernst et al., 1997; Froitzheim et al., 2003; Hacker & Gerya, 2013; Liou et al., 2004; Majka et al., 2014; Platt, 1993; Warren, 2013). One important realization of the discussion is that exhumation is initially driven by buoyancy forces arising from the juxtaposition of continental crust against the mantle. This can result in plate velocity-scale (up to 1–2 cm/yr) exhumation from UHP depths to crustal levels (e.g., Rubatto & Hermann, 2001). As the material arrives at middle crustal levels, buoyancy forces acting on the exhuming continental crust become dampened and other mechanisms such as extrusion, shear traction or extension are required for the final exhumation stages (Carswell et al., 2003; Parrish et al., 2006; Rubatto & Hermann, 2001; Terry et al., 2000; Warren, 2013).

The application of geochronological tools, such as white mica $^{40}Ar/^{39}Ar$ geochronology, is crucial for understanding dynamic exhumation of UHP continental rocks. White mica is typically a major phase within metasedimentary lithologies of continental affinity, and often defines, or is genetically associated with, tectonic structures that facilitates exhumation. In recent years, there have been significant advancements for $^{40}Ar/^{39}Ar$ geochronology with regard to our understanding of ^{40}Ar diffusion mechanisms and

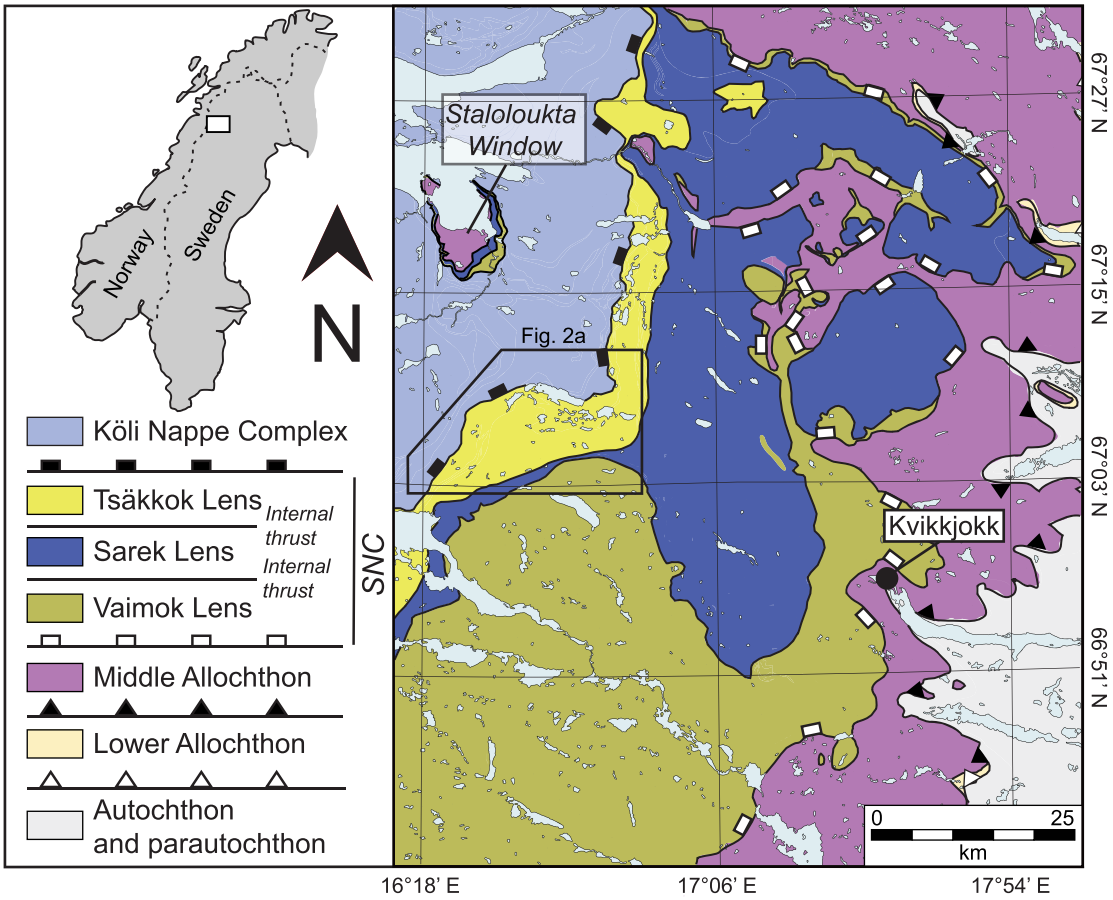

Figure 1. Simplified tectonostratigraphic map of the Scandinavian Caledonides in southern Norrbotten, Sweden, based on a map by Thelander (2009). The white rectangle in the inset map demarcates the approximate location of the field area with respect to Sweden and Norway. The black box indicates the location of Figure 2. The village of Kvikkjokk is labeled as a reference point for the field area. Abbreviation: SNC, Seve Nappe complex.

an increase in sensitivity and mass resolution in instrumental analyses. Some studies have demonstrated that diffusion of ^{40}Ar from white mica can be dependent on crustal pressure conditions in addition to temperature (Harrison et al., 2009; Warren et al., 2012). Therefore, ^{40}Ar diffusion in white micas in UHP rocks may close at temperatures up to 500°C. Furthermore, ^{40}Ar loss from white micas can be driven by recrystallization/neocrystallization during deformation occurring at pressure and temperature conditions that is not conducive for thermally activated diffusive loss (i.e., below the closure temperature; e.g., Cosca et al., 2011; Cossette et al., 2015; Egli et al., 2017; Kellett et al., 2016; Kramar et al., 2001; Mulch & Cosca, 2004; Schneider et al., 2019). Application of in situ ^{40}Ar/^{39}Ar geochronology enables the structures of deformed rocks to be directly dated, allowing the possibility to decode cooling and deformation processes during incipient to late stage exhumation of UHP rocks. Therefore, combining in situ white mica ^{40}Ar/^{39}Ar geochronology with detailed structural analyses can reveal powerful information about both the exhumation and deformation history of UHP continental rocks.

Our approach combines macrostructural and microstructural investigations with in situ white mica ^{40}Ar/^{39}Ar and electron microprobe (EMP) analyses to the high-pressure (HP) Tsäkkok Lens in the Seve Nappe Complex (SNC) of the Scandinavian Caledonides (Figures 1 and 2). The SNC provides a >1,000-km orogen-parallel record of continental rocks that were subducted to, and exhumed from, UHP conditions (e.g., Andréasson & Gee, 1988; Brueckner & van Roermund, 2004; Bukała et al., 2018; Gee et al., 2013; Janák et al., 2013; Klonowska et al., 2014, 2016, 2017; Majka et al., 2014; Petrík et al., 2019; Stephens & van Roermund, 1984; van Roermund, 1985, 1989). The exposure and rock record of the SNC thus provides an excellent natural laboratory for developing geodynamic models for the subduction-exhumation cycle of continental crust along the length of a continental collisional zone. Understanding the structural style, timing, and rates of exhumation

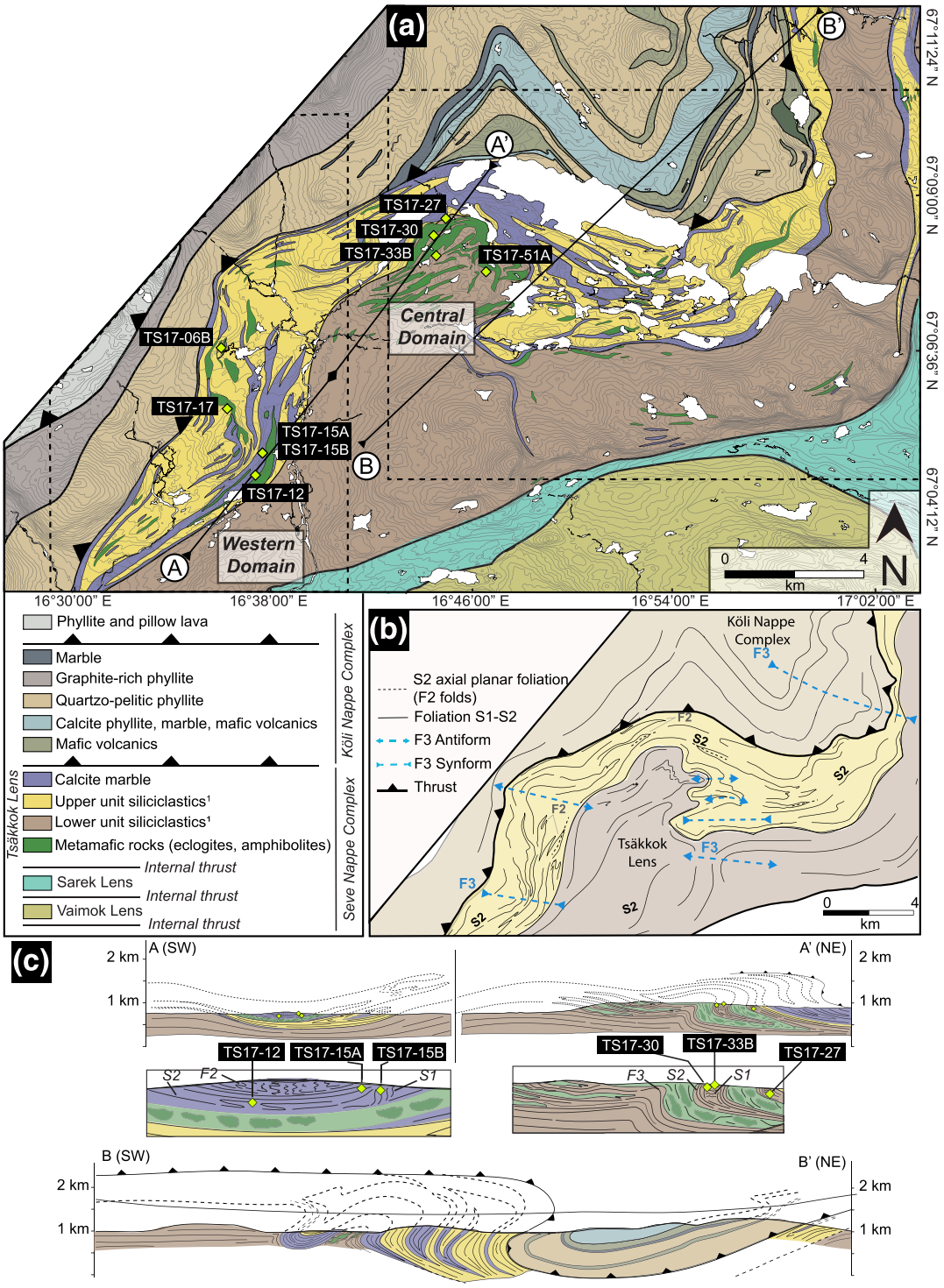

Figure 2. (a) Tectonostratigraphic map of the Tsäkkok Lens and the overlying Köli Nappe complex and corresponding legend, based on the maps of Kullerud (1987) and Snilsberg (1987). Yellow diamonds indicate the locations of samples collected from the western and central domains. Dashed boxes represent the locations shown in Figure 4. (b) Simplified map showing the bulk architecture and main structural trends of the Tsäkkok Lens and Köli Nappe complex. (c) Geological cross sections (marked as solid black lines in Figure 2a) through the Tsäkkok Lens and overlying Köli Nappe complex. The cross sections illustrate the reorientation of D1 and D2 structures by F3 folds and the combined folding of the Tsäkkok Lens within the Köli Nappe complex. Representative sample locations (yellow diamonds) are plotted within the A-A′ cross section for some of the samples obtained from S1 and S2 in the western and central domains. No vertical exaggeration is depicted in the cross sections. [1]Refer to the geological background section for descriptions of the upper and lower unit siliciclastic sequences.

for the Tsäkkok Lens is critical for development of geodynamic models of the SNC, which has implications for the evolution of the Scandinavian Caledonides. The results reported here elucidate a protracted exhumation history from eclogite-facies conditions to shallow-crustal levels. This provides the basis for further studies of other tectonic lenses that are tectonostratigraphically correlated (the UHP Vaimok and amphibolite-facies Sarek lenses; Figure 1). The collective results can then be synthesized with respect to other key UHP localities along strike of the SNC, such as the Kebnekaise mountain region to the northeast (e.g., Andréasson et al., 2018) and the Jämtland localities to the southwest (e.g., Brueckner & van Roermund, 2004; Janák et al., 2013; Klonowska et al., 2014, 2016, 2017; Majka et al., 2014), to contribute to the development of geodynamic models for the subduction-exhumation process of continental crust.

2. Geological Setting

The Scandinavian Caledonides record the closure of the Iapetus ocean, culminating in continental collision of Baltica with Laurentia (e.g., Gee et al., 2008). The Caledonides are generally divided into (para-)autochthonous Baltican basement, which is overlain by the Lower, Middle, Upper, and then Uppermost Allochthons (e.g., Gee et al., 1985; Stephens et al., 1985), although the some oversimplifications of these divisions have been questioned (Corfu et al., 2014). Of these allochthons, UHP rocks are prominent in the SNC of the Middle Allochthon (e.g., Gee et al., 2013, 2020). The SNC comprises metasedimentary and metaigneous rocks that represent the extended passive margin of Baltica (e.g., Andréasson et al., 1992; Jakob et al., 2019; Kjøll et al., 2019). These rocks were subducted to mantle depths beneath a volcanic arc of Iapetus affinity during Caledonian orogenesis (e.g., Andréasson, 1987; Brueckner & van Roermund, 2004; Bukała et al., 2018; Gee, 1975; Janák et al., 2013; Klonowska et al., 2014, 2016, 2017; Kullerud et al., 1990; Majka et al., 2014; Petrík et al., 2019; Santallier, 1988; Stephens & van Roermund, 1984).

A key SNC locality of UHP continental rocks resides in southern Norrbotten, Sweden (Figure 1). This SNC locality is traditionally subdivided into three tectonic mega-lenses (Zachrisson & Stephens, 1984): the eclogite-facies Vaimok Lens, the amphibolite-facies Sarek Lens, and the eclogite-facies Tsäkkok Lens (Figure 1). The Tsäkkok Lens is further divided into two lithostratigraphic subunits, the lower and upper Tsäkkok units (Kullerud, 1987; Snilsberg, 1987; Figures 2a and 2b). The lower unit is predominantly composed of well-foliated quartzofeldspathic gneiss with a lesser abundance of (garnet-)white mica schists, whereas the upper unit is more heterogeneous in nature with marbles, calcareous schists, and (garnet-)white mica schists (Kullerud, 1987). Eclogite bodies in the Tsäkkok Lens range in length from a few cm up to ~100 m and are typically concordantly elongated with the main, regional foliation. These bodies are hosted within both the siliciclastic and carbonaceous metasediments and can be found within both the upper and lower units of the Tsäkkok Lens, although they are more abundant in the upper unit where they are frequently localized in discrete horizons (Figure 2c). Locally, some eclogites preserve pillow basalt textures (Kullerud et al., 1990). The mixture of continentally derived rocks, marbles, and the intrusions of the mafic bodies into the metasediments as well as submarine volcanism had led to the interpretation that the Tsäkkok Lens represents a hyper-extended portion of the Baltican passive margin, bordering the Iapetus Ocean (Kjøll et al., 2019; Kullerud et al., 1990).

Peak metamorphic conditions of the Tsäkkok Lens eclogites were constrained by garnet-clinopyroxene geothermobarometry, which yielded a minimum pressure of 14.9 kbar and a temperature of 610 ± 90°C (Stephens & van Roermund, 1984). A more recent investigation has updated the P-T estimates to ~22 kbar and ~590°C (Bukała et al., 2020). Peak conditions were then followed by an exhumation pathway that was initially defined by nearly isothermal decompression (Kullerud, 1987). The conditions for retrogressive metamorphism and development of an exhumation-related foliation in the metasedimentary rocks are broadly constrained from ~10 kbar and ~500°C, down to ~6 kbar and ~400°C (Snilsberg, 1987). Mørk et al. (1988) pioneered the first geochronological study of the Tsäkkok Lens obtaining a garnet-omphacite-whole rock Sm-Nd isochron date of 505 ± 18 Ma (2σ), interpreted to represent the age of eclogite-facies metamorphism. More recently, isotope dilution thermal ionization mass spectrometry U-Pb geochronology of zircon obtained from one eclogite exposure in the Tsäkkok Lens obtained a younger date of 481.9 ± 1.1 Ma (2σ; Root & Corfu, 2012), which was also interpreted to reflect the timing of eclogite-facies metamorphism. Root and Corfu (2012) regarded the discrepancy between the two studies to reflect disequilibrium of the Sm-Nd system in the sample dated by Mørk et al. (1988). Exhumation from peak conditions was dated via

Table 1
Summary of the Rock Samples, Locations, Associated Deformation Structures, and the Results of Electron Microprobe and White Mica $^{40}Ar/^{39}Ar$ Geochronological Analyses

Sample	Rock type	Coordinates[a]	Notable structures	D2 coaxial/ noncoaxial	White mica compositions	$^{40}Ar/^{39}Ar$ date ranges	$^{40}Ar/^{39}Ar$ age populations ($\pm 2\sigma$)[b]
S1							
TS17-15B	Metapsammite	67°05′21.46″N 16°37′50.86″E	N/A	N/A	XMs: 0.35–0.41 XCel: 0.51–0.56	circa 485–469 Ma	489.8 ± 8.6 Ma; 477.2 ± 4.1 Ma;
TS17-27	Metapelite	67°08′55.14″N 16°45′24.94″E	F2 folds; weak S2 foliation development	Coaxial	XMs: 0.59–0.67 XCel: 0.15–0.25	circa 487–459 Ma	458.1 ± 9.0 Ma
TS17-30	Metapelite	67°08′39.61″N 16°44′54.65″E	Symmetrical F2 folds and strain shadows around garnet	Coaxial	N/A	circa 494–448 Ma	
TS17-33B	Metapelite	67°08′20.76″N 16°44′59.35″E	Symmetrical F2 folds	Coaxial	XMs: 0.45–0.49 XCel: 0.39–0.43	circa 496–476 Ma	
S2							
TS17-06B	Metapsammite	67°07′0.26″N 16°36′19.18″E	Anastomosing shear bands	Coaxial and noncoaxial	XMs: 0.43–0.49 XCel: 0.25–0.29	circa 487–471 Ma	495.8 ± 8.8 Ma; 475.3 ± 3.5 Ma;
TS17-12	Metapsammite	67°05′1.09″N 16°37′33.41″E	Anastomosing shear bands; asymmetrically transposed relic S1	Noncoaxial	XMs: 0.48–0.62 XCel: 0.11–0.38	circa 494–424 Ma	446.3 ± 6.3 Ma; 429.6 ± 12.0 Ma
TS17-15A	Metapsammite	67°05′21.46″N 16°37′50.86″E	Mica fish, asymmetrically transposed relic S1	Noncoaxial	XMs: 0.50–0.68 XCel: 0.14–0.34	circa 505–426 Ma	
TS17-17	Metapelite	67°06′3.63″N 16°36′29.35″E	Symmetrical strain shadows around garnet	Coaxial	XMs: 0.50–0.56 XCel: 0.24–0.28	circa 494–471 Ma	
TS17-51A	Metapsammite	67°08′8.01″N 16°46′58.36″E	Mica fish	Noncoaxial	XMs: 0.54–0.64 XCel: 0.11–0.28	circa 480–439 Ma	

[a]Using WGS geographic coordinate system. [b]Age populations calculated using the Gaussian deconvolution method.

$^{40}Ar/^{39}Ar$ step heating of hornblende and white mica (Dallmeyer & Stephens, 1991), yielding dates of 464.7 ± 1.3 and 463.2 ± 6.3 Ma, and 468.4 ± 0.9 and 448.2 ± 1.6 Ma (2σ), respectively. These dates were interpreted as cooling during protracted exhumation of the Tsäkkok Lens through moderate temperatures (500–300°C).

The Tsäkkok Lens is tectonically overlain by the Köli Nappe Complex (KNC) of the Upper Allochthon (Figure 1). Generally, the KNC in Norrbotten comprises metamorphosed sediments and volcanic and intrusive rocks (Pedersen et al., 1991; Stephens, 1980, 2020; Stephens et al., 1985). Collectively, this package of rocks represents the relics of the Iapetus Ocean beneath which the SNC was subducted (Gee et al., 2013; Stephens, 1988) during closure of the ocean basin that culminated in continental collision between Baltica and Laurentia (Gee et al., 2008; Stephens et al., 1985).

3. Methodology

Fieldwork was conducted in the western and central domains of the Tsäkkok Lens to investigate the macroscale to mesoscale structures of the lens and to obtain measurements for resolving the structural evolution. Our measurements were supplemented by those of Kullerud (1987) and Snilsberg (1987). Multiple samples of structures of different generations were obtained across the western and central domains of the lens, and these samples were utilized for detailed microstructural investigation. Of these, nine key samples were chosen for in situ white mica $^{40}Ar/^{39}Ar$ geochronology to resolve the tectonic evolution of the lens (Figure 2 and Table 1). Glass-mounted, polished thick sections (~500 μm) were prepared from the nine key samples. The selected areas of interest on the thick sections were photographed using back-scattered electron (BSE) imaging and X-ray mapped for major elements (Si, Al, Mg, Fe, and K) using wavelength-dispersive spectrometry (WDS) on an EMP. After imaging was completed, the thick sections were gently repolished to remove the carbon coating prior to irradiation and dating. Eight of the nine samples were chosen for quantitative EMP WDS spot analyses on polished ~30-μm thin sections that "mirrored" the thick sections, to avoid volatilization of elements (e.g., K) in the white micas from the $^{40}Ar/^{39}Ar$ thick sections. These WDS spot analyses targeted white micas with the same structural positions that were chosen for $^{40}Ar/^{39}Ar$ geochronology. The WDS analyses were located in the central portions of the grains, away from the white mica grain boundaries to avoid geochemical effects of white mica replacement by biotite or chlorite. The WDS X-ray mapping

of the thick sections and WDS spot analyses on the thin sections were conducted using a JEOL JXA8230 EMP at AGH University of Science and Technology (Kraków, Poland). The EMP was operated using an accelerating voltage of 15 kV and a beam current of 50 nA, with a 5-μm spot size for WDS analyses.

In situ $^{40}Ar/^{39}Ar$ analytical work was performed at the University of Manitoba (Winnipeg, Canada) using a multicollector Thermo Fisher Scientific ARGUS VI mass spectrometer, linked to a stainless steel Thermo Fisher Scientific extraction/purification line and Photon Machines (Analyte Excite) 193-nm laser. The technical details of the $^{40}Ar/^{39}Ar$ methods are available in the supporting information Text S1. Depending on the shape of the white mica grain, a raster size of 100 × 100 μm or 50 × 200 μm was used. Pit depths were estimated to be ~50 μm. Both the BSE images and the X-ray elements maps were used to target structural areas of interest for in situ $^{40}Ar/^{39}Ar$ analyses and for quality control of the laser spot placement. Analytical targets were placed using X-ray mapped regions or areas identified from BSE imaging. The locations of the in situ $^{40}Ar/^{39}Ar$ analyses were targeted in the centers of grains to avoid possible chemical zoning of the white micas due to biotite or chlorite replacement.

4. Results

4.1. Macrostructural Analysis

The architecture of the NE-SW trending Tsäkkok Lens is interpreted to be the result of the superposition of three deformation events (D1, D2, and D3; Figures 2b and 2c). Structures associated with D1 deformation are typically preserved in the microscale to mesoscale (i.e., thin section to outcrop scale), whereas D2 and D3 structures are readily observed from the mesoscale to macroscale (i.e., outcrop to regional scale). The internal architecture of the Tsäkkok Lens is predominantly defined by D2 structures in addition to subordinate D1 and D3 structures (Figures 2b and 2c). However, the general architecture of the lens is governed by a km-scale, asymmetric Z-folding associated with D3 deformation (Figures 2b and 2c), which deformed the KNC-Tsäkkok and Tsäkkok-Sarek thrust boundaries. Microscale to macroscale structural analysis has been conducted using outcrop observations in the western and central domains of Tsäkkok Lens and published maps.

D1 deformation is represented as an S1 foliation that is locally preserved in carbonaceous and siliciclastic metasedimentary rocks in both western and central domains of the Tsäkkok Lens (Figures 2c and 3a–3c). In the carbonaceous metasediments, the foliation is defined by silica-rich laminae, whereas in the siliciclastic metasediments it is defined by quartz-rich layering and the alignment of white micas. S1 is best preserved as microlithons within S2 (Figure 3b) or in areas with abundant eclogite bodies. In eclogite-rich areas, the S1 either shows no indications of D2 deformation overprint (Figure 3c) or is folded by F2 (Figures 3a and 3b). No lineations nor kinematic indicators have been found associated with S1.

In both the western and central domains, D2 structures are defined by S2 and closed to isoclinal folds (F2; Figures 2b, 2c, and 3). S2 is the dominant foliation of the Tsäkkok Lens and trends parallel to the bulk architecture (Figure 2b). Similar to S1, S2 is predominantly defined by subordinate silica-rich layering within the carbonaceous metasediments and by the alignment of white micas and quartz banding in siliciclastic metasediments. Where preserved on the mesoscale, S1 is observed to be oriented at a high angle to S2 (Figures 3b and 3c). In one instance in the western domain, an outcrop of vertical S1 (TS17-15B) is flanked by two eclogite bodies and is located a few tens of meters downslope from an exposure of the subhorizontal S2 (TS17-15A; Figure 3c). In low-strain D2 zones, the preserved S1 is folded on the cm- to m-scale by closed F2 and is observed to be transposed into S2 (Figures 3a and 3b). Some outcrops that preserve S1 folded by F2 also exhibit a weak development of S2 parallel to the axial planes of F2 (Figure 3a). In high-strain D2 zones, S2 has completely overprinted S1. Isoclinal folds are common in D2 high-strain zones with axial planes parallel to S2 (Figure 3d). A strong white mica L2 stretching lineation is also present, trending WNW-ESE (Figure 4). Structures indicative of noncoaxial deformation are readily observed in the high-strain zones. Mesoscale sheath folds are common in high-strain zones (e.g., Snilsberg, 1987). Flanking folds associated with rotated slip planes are also locally observed (Figure 3e). These structures provide a top to east sense of shear during D2 deformation.

The S2 foliation is observed to be deflected around eclogite bodies that are hosted in the metasediments. The amphibolitized margins of the eclogite bodies also record a foliation that is concordant with S2 and are often infolded with F2 (Figure 3f). These F2 folds are typically cm- to m-scale closed folds possibly representing

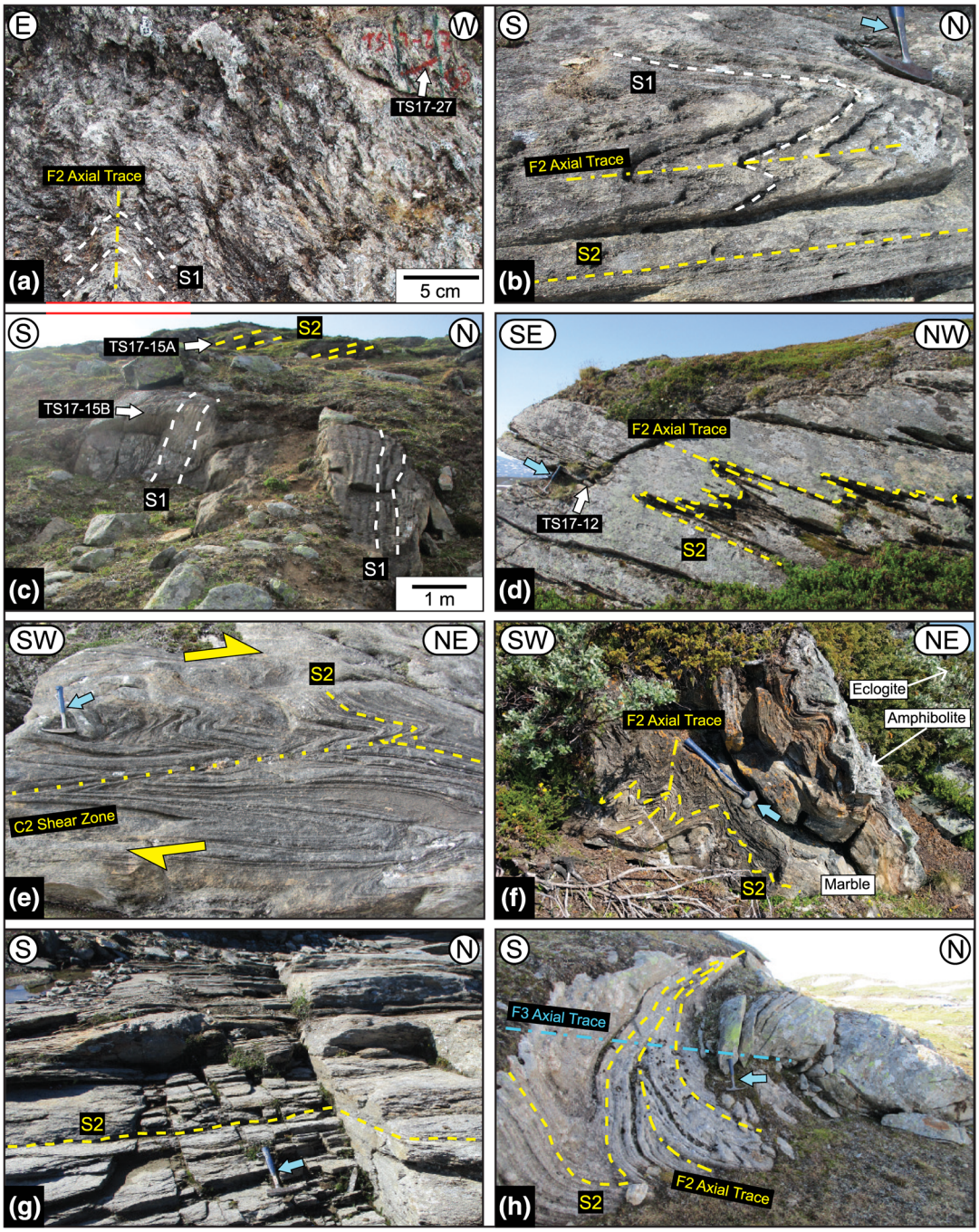

Figure 3. Field photographs of key outcrops illustrating the progressive evolution of structures for the Tsäkkok Lens. (a, b) Folding of S1 by F2 in both a) metapelites of the central domain and (b) metapsammites of the western domain. In (a), the white arrow denotes the sample location of TS17-27. S1 = 240/55°NW; S2 = subvertical striking 10–190°. The light blue arrows in Figures 3a and 3d–3h points to hammers that are used for scale. In (c), F2 is preserved in low-strain domains, whereas high-strain domains are defined by the horizons of the S2 (bottom). S2 = 222/29°NW. (c) An outcrop of interlayed metapsammites and marbles in the western domain showing the vertical S1 (TS17-15B shown by a white arrow; S1 = 085/69°S) that is bounded on both sides by eclogite boudins. Upslope from this site are outcrops of shallowly dipping S2 (TS17-15A; S2 = 169/32°W), demonstrating the perpendicular relationship between the two orientations. (d) Metapsammite outcrop showing F2 drag folds within a high D2 strain outcrop (TS17-12 shown by a white arrow) in the western domain (S2 = 231/24°NW; F2 axial plane = 280/20°N). (e) F2 flanking folds distorting S2 around a rotated slip plane, with the orientation providing a top to east sense of shear. (f) Marbles folded together with the amphibolitized margin of an eclogite body. Folds are classified as F2 and may represent quarter structures developed around the rigid eclogite body. It is unclear if the slight fold of the F2 axial plane is due to F3 folding or later-staged distortions of F2 during progressive D2 deformation. (g) Phyllonitic rocks associated with the tectonic contact between the Tsäkkok Lens and the overlying Köli Nappe complex in the western domain (S2 = 190/22°W). (h) F3 folds within a metapsammite outcrop that have refolded F2 in the central domain of the Tsäkkok Lens, representing the final stage of deformation (F3 axial plane = 207/22°NW). Light blue arrows indicate where hammers are used for scale.

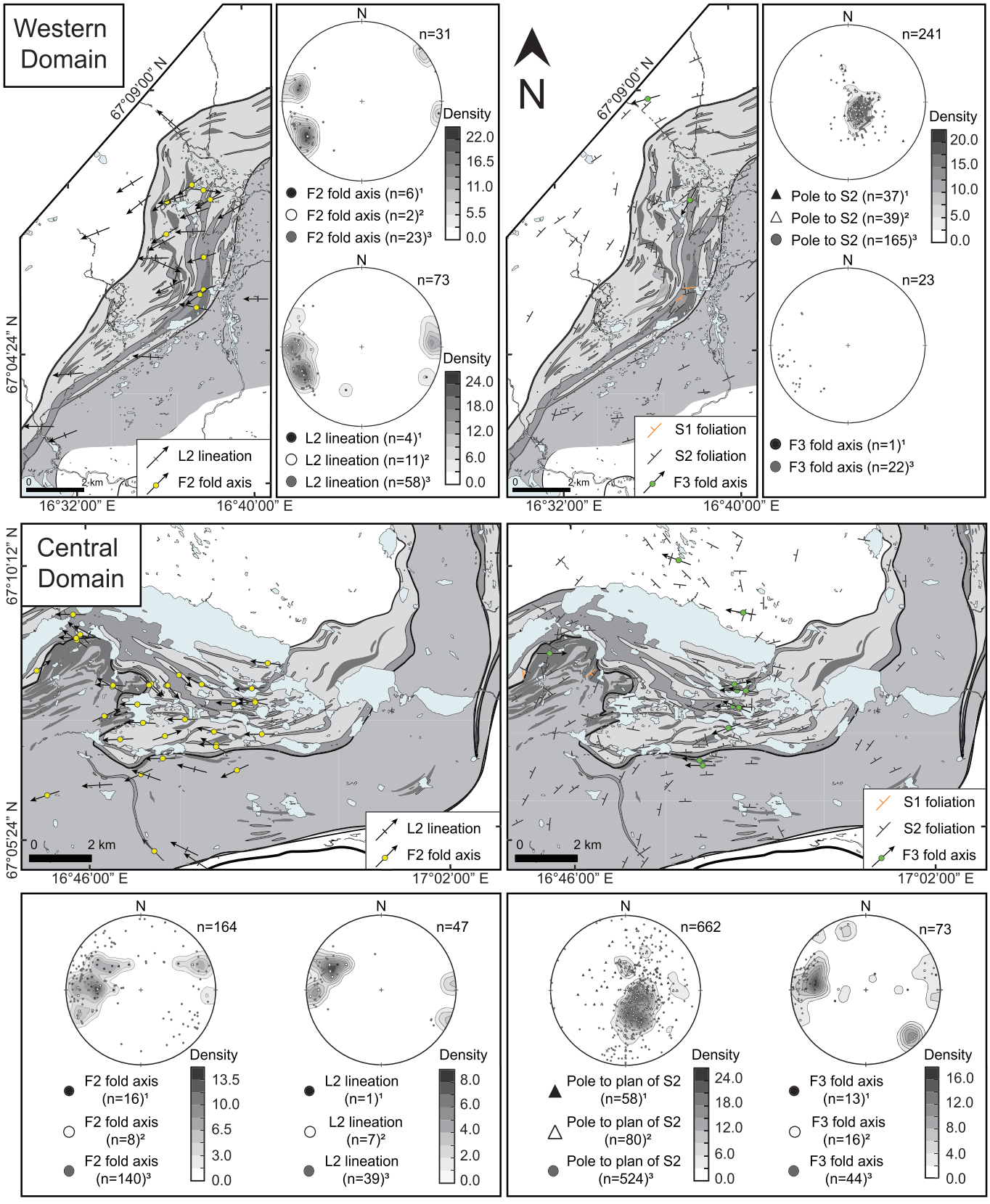

Figure 4. Simplified tectonostratigraphic maps annotated with planar and linear structural data and associated lower hemisphere stereonets for the western domain (top) and the central domain (bottom) of the Tsäkkok Lens. Data points are compiled from this study[1], Kullerud (1987)[2], and Snilsberg (1987)[3].

quarter structures developed around a rigid eclogite body (Fossen et al., 2018). However, the infolded metasedimentary rocks and amphibolitized margins were only partially exposed, preventing complete observation of the contact. The eclogite bodies that were not subjected to amphibolitization do not exhibit any foliation nor folding. The thrust contact between the Tsäkkok Lens and overlying KNC is characterized by greenschist-facies phyllonites and high-strain marbles (Figure 3g). The penetrative foliation of the thrust zone is parallel with S2 defined in the Tsäkkok Lens (e.g., Stephens et al., 1985).

D3 deformation is defined by F3, open antiformal and synformal folds that are both at the km-scale (Figures 2b and 2c) and m-scale (Figure 3h). The NE-SW central domain represents a steeply dipping to overturned limb of an open F3 synform-antiform pair (Figure 2c). The m-scale folds are abundant within the central domain where they refold mesoscale F2 structures (Figure 3h). F3 are not as clearly recognized within the western domain. A local, weak S3 foliation development was reported by Kullerud (1987), but no such foliation was observed during this study.

F3 folding of the Tsäkkok Lens transposed structures relating to both D1 and D2 deformation events (Figures 2b, 2c, and 3h). In the western limb, S1 is generally observed to be subvertical, whereas S2 is observed to be dipping ~20–30° to the NW (Figures 2c and 4). Within the central domain (the overturned limb of the F3 synform-antiform pair) F3 folding reoriented S1 and S2, such that S1 is observed to be moderately dipping (Figures 2c and 4). S2 shows a large dispersion in orientations largely due to the abundance of eclogite bodies, around which S2 is deflected, as well as the pervasive F3 folding in the central domain (Figure 4). As a result, both elements of a moderately NW dipping and nearly subvertical S2 are present. In both domains, a perpendicular relationship between S1 and S2 is recognizable. The orientations of F2 axes and the L2 stretching lineations do not differ as dramatically from the western to the central domain (Figure 4). In the western domain, they are generally oriented WSW-ENE. In the central domain, they are oriented with a WNW-ESE trend and still predominantly plunge toward the west (Figure 4). F3 fold axes are also generally parallel to the F2 fold axes and L2. However, the F3 folds have refolded the F2 axial planes, defining Type-3 refold structures (Ramsay, 1967). The axial planes of F2 in the western domain are often oriented subvertically (parallel with S2), whereas the F3 axial planes are subvertical. In the central domain, the opposite orientations are predominantly recognized with subvertical F2 axial planes and subhorizontal F3 axial planes (Figures 3h and 4).

4.2. Microstructural Analysis

Nine strategically chosen samples from the upper and lower units of the Tsäkkok Lens were characterized for petrographic and microstructural features. The samples were primarily targeted based on their specific structures (Figure 5 and Table 1): relic S1 (TS17-15B), S1 folded by F2 (TS17 to TS1727, TS17-30, and TS17-33B), and S2 (TS17-06B, TS17-12, TS17-15A, TS17-17, and TS17-51A). The samples are broadly categorized either as metapsammites (e.g., quartzofeldspathic gneisses; TS17-06B, TS17-12, TS17-15A, TS17-15B, and TS17-51A) or metapelites (e.g., calcareous and noncalcareous white mica schists, TS17-17, TS17-27, TS17-30, and TS17-33B). The metapsammites are generally quartz-dominated with relatively minor white mica ± calcite, plagioclase, clinozoisite, garnet, apatite, or zircon. The foliations in the metapsammites are predominantly defined by quartz bands separated by thin (10–50 μm) to thick (0.4–3 mm) continuous layers of white mica. Metapelitic rocks are dominated by foliation-defining white mica with relatively minor quartz ± plagioclase, clinozoisite, garnet, apatite, zircon, allanite, or monazite. Where monazite is found in S1 (TS17-27), the crystals are large (up to 300-μm diameter) and do not show signs of retrogression. The samples containing S2 preserve small (up to 20-μm diameter) relics of monazite that are mantled by apatite, allanite, and clinozoisite, demonstrating retrogression of monazite (e.g., Janots et al., 2007; Spear, 2010). Localized, partial replacement of white mica by either biotite or chlorite is observed in all of the samples. Some biotite and chlorite are also present as individual crystals, although these comprise a minor (<10%) fraction of the total mica population.

Investigation of the microstructures associated with S1 and S2 reveals variations in the strain characteristics among the samples. One sample (TS17-15B) obtained from between two eclogite bodies (Figure 3c) is characterized by S1 that is not overprinted by D2 deformation. However, three more samples that contain S1 (TS17-27, TS17-30, and TS17-33B) are folded by F2. Among these samples, plagioclase porphyroblasts are present, either found as rounded (TS17-33B; Figure 5a) or as elongated agglomerations of smaller crystals (Figures 5b and 5c). The rounded porphyroblasts include white micas that are concordant with S1 folded

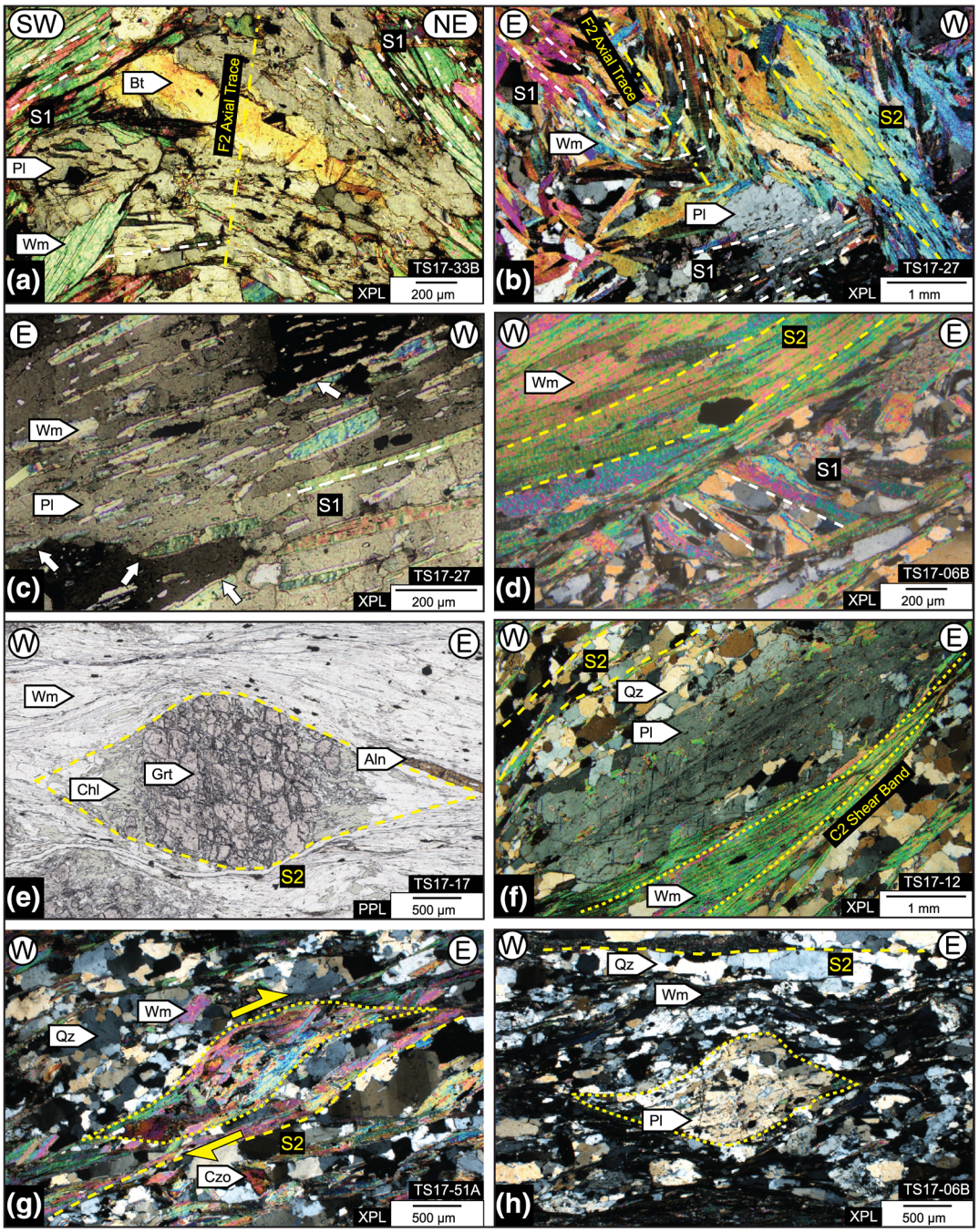

Figure 5. Photomicrographs of key metasedimentary rock microstructures. (a) Unstrained plagioclase porphyroblast overprinting the apex of F2. White mica inclusions record both orientations of the folded S1 culminating in the fold apex. (b) S1 in Sample TS17-27 folded by F2. The plagioclase porphyroblast exhibits undulose extinction and subgrain formation, which preserves prefolded S1. Recrystallized plagioclase grain boundaries are pinned against the white micas of the prefolded S1. A weak S2 axial planar foliation is developed perpendicular to the prefolded S1. (c) Magnified image of the plagioclase porphyroblast preserving S1 seen in photomicrograph (b). White arrows mark the locations where the plagioclase subgrains are pinned against white mica inclusions. (d) S2 within low-strain polymineralic lenses in Sample TS17-06B. Preservation of small pockets of S1 perpendicular to S2, which are not transposed into S2. (e) Symmetrical strain shadow around garnet porphyroblast in Sample TS17-17. The garnet is partially decomposed to chlorite, which also partially infills the strain shadows. Elongate allanite (after monazite) is observed parallel to the S2 foliation. (f) S2 and C2 shear bands in Sample TS17-12. White mica crystals are concordant to the shear bands and are deformed. The plagioclase porphyroblast includes white mica inclusions that are parallel to S2. The boundaries of the plagioclase show undulose extinction and subgrain development, with grain boundaries pinned again the white mica inclusions. (g) White mica fish bundle deformed along S2 in Sample TS17-51A. The mica fish bundle provides a top to east sense of shear. (h) Sigmoidal plagioclase porphyroclast in a high-strain S2 domain from Sample TS17-06B. Shear bands are parallel to S2. Inclusions forming an S-shaped trail are outlined. Abbreviations: Aln, allanite; Bt, biotite; Chl, chlorite; Czo, clinozoisite; Grt, garnet; Pl, plagioclase; Qz, quartz; Wm, white mica; XPL, cross-polarized light; PPL, plane-polarized light.

by F2 and are moderately strained with development of subgrain boundaries and minor moderate undulose extinction. In contrast, the elongated porphyroblasts preserve significant undulose extinction and pervasive subgrain boundary development (Figure 5c). Many of the small, individual plagioclase boundaries are observed to be pinned against white mica. These white micas are generally aligned with white mica found within the hinges of F2 and are perpendicular to an incipient S2, where present (TS17-27; Figure 5b).

Samples containing S2 contain both coaxial and noncoaxial structures. The samples with coaxial structures (TS17-06B and TS17-17) predominantly contain nontransposed relic S1 (TS17-06B; Figure 5d) or symmetrical strain shadows that surround partially chloritized garnet porphyroblasts (TS17-17; Figure 5d) as well as chlorite pseudomorphs after garnet (sometimes containing garnet remnants; TS17-30). In some samples, noncoaxial structures are observed (TS17-06B, TS17-12, TS17-15A, and TS17-51A), which are locally observed to overprint coaxial structures (e.g., TS17-06B). These structures typically comprise anastomosing μm-scale C2 shear bands defined by white mica or chlorite. The anastomosing nature of the shear bands defines polymineralic lenses (up to 1 cm thick) that are dominated by quartz and also contain white mica and plagioclase. Internally in these lenses, white mica tends to be coarser and significantly less deformed (Figure 5d) than the white micas associated with the shear bands (Figure 5f). Bundles of white mica adjacent to the shear bands are deformed and deflected concordantly with the shear band trajectories (TS17-12; Figure 5f). More localized shear band development creating mica fish structures can also be observed within some samples (TS17-15A and TS17-51A). These mica fish structures display a top to east sense of shear (Figure 5g). Pockets of S1 are locally observed to be deflected and asymmetrically transposed into the dominant S2 (TS17-12 and TS17-15A).

In plagioclase-bearing samples that are characterized by noncoaxial structures, the plagioclase can either be found within high-strain horizons (TS17-06B; Figure 5h) or in the polymineralic lenses that are defined by the anastomosing shear bands (TS17-12; Figure 5e). Plagioclase in the high-strain horizons are deformed along μm-scale C2 shear bands with a sigmoidal structure akin to mica-fish (Figure 5h). Internally, these grains exhibit undulose extinction and subgrain development. Plagioclase in polymineralic lenses are elongated parallel to S2 and contain aligned inclusions of white micas that are also parallel to S2. The plagioclases are relatively strain free with the exception of the grain margins that show undulose extinction, subgrain development, pinning structures against white mica, and localized lamellar twinning.

4.3. White Mica Geochemistry

Following the method of Coggon and Holland (2002), the results of the white mica WDS spot analyses were recalculated to nine mica endmember compositions (Table S1). For the calculations, the content of ferric iron in the white mica grains was considered to be 0. The results show a large range in both the muscovite (X_{Ms}) and celadonite ($X_{Cel} = X_{MgCel} + X_{FeCel}$) endmembers that range between 0.35–0.68 and 0.08–0.56, respectively (Figures 6 and 7 and Table S1). The results show an increasing paragonite endmember component (X_{Pa}) that ranges from 0.00–0.32 with increasing X_{Ms}. A component of the phlogopite endmember (X_{Phl}) is also present, up to 0.15 X_{Phl}. There are significant intrasample differences with regards to the ranges in X_{Ms} and X_{Cel}, which can be readily observed in the qualitative X-ray major element maps (Figures 6 and 7). Two samples of S1 show a small scatter of X_{Ms}: 0.35–0.41 and X_{Cel} = 0.51–0.56 (TS17-15B) and X_{Ms} = 0.45–0.49 and X_{Cel} = 0.39–0.43 (TS17-33B), whereas one more sample of S1 shows a moderate dispersion of X_{Ms} = 0.59–0.67 and X_{Cel} = 0.15–0.25 (TS17-27). The samples containing coaxial S2 exhibits clusters of X_{Ms} = 0.43–0.49 and X_{Cel} = 0.25–0.29 (TS17-06B) and X_{Ms} = 0.50–0.56 and X_{Cel} = 0.24–0.28 (TS17-17). In contrast, the three samples containing noncoaxial S2 exhibit large scatter of X_{Ms} = 0.48–0.62 and X_{Cel} = 0.11–0.38 (TS17-12), X_{Ms} = 0.50–0.68 and X_{Cel} = 0.14–0.34 (TS17-15A), and X_{Ms} = 0.54–0.64 and X_{Cel} = 0.11–0.28 (TS17-51A).

4.4. White Mica Geochronology

A total of 55 in situ ultraviolet (UV) laser spot dates was obtained from nine samples (Table S2). The analyses all contain radiogenic ^{40}Ar ($^{40}Ar^*$) values >97%, with the exception of a value of 89.3% from Sample TS17-06B and 94.6% from Sample TS17-17. No significantly high Cl/K ratios were observed for any analyses. The Ca/K ratios range from 0.00 to 1.09, indicating the presence of a Ca-bearing phase in some of the analyses. However, there are is no systematic correlation between the Ca/K ratios and the reported $^{40}Ar/^{39}Ar$ dates, indicating that contamination of the analyses was negligible.

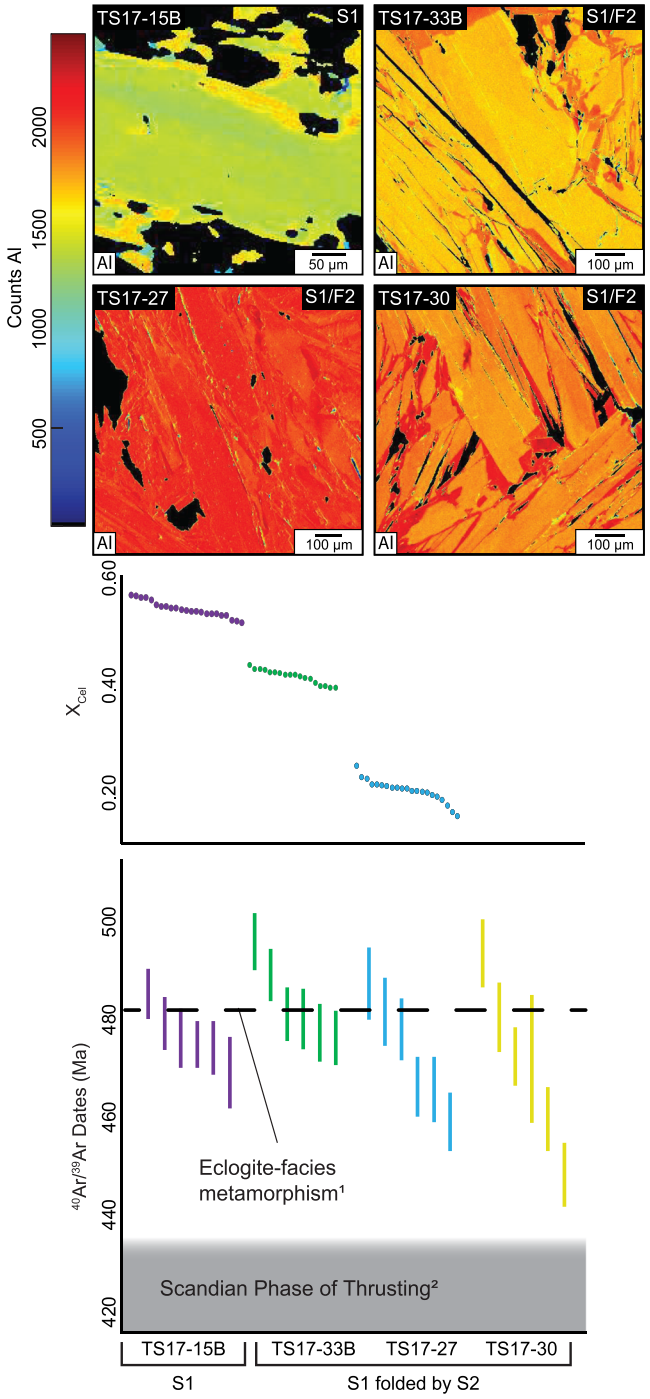

Figure 6. Qualitative electron microprobe X-ray chemical maps of Al (top) and quantitative wavelength-dispersive spectroscopy geochemical results (X_{Cel}) with $^{40}Ar/^{39}Ar$ dates (bottom) for samples containing S1. The chemical maps were used for dating and depict white micas that were analyzed for $^{40}Ar/^{39}Ar$ geochronology. One representative chemical map is presented for each sample, categorized based on the microstructures. Minerals other than white mica in the maps were masked using XMapTools v. 2.6.4 (Lanari et al., 2014). The individual $^{40}Ar/^{39}Ar$ dates ($\pm 1\sigma$ uncertainties) are plotted for each sample below the quantitative geochemical data, with the exception of Sample TS17-30, for which no geochemical data were obtained. The analyzed samples are classified according to their microstructures. The timing of eclogite facies metamorphism [1](Root & Corfu, 2012) and the timing of Scandian thrusting [2](Andréasson et al., 2018; Bender et al., 2019; Dallmeyer, 1990; Dallmeyer & Gee, 1988; Grimmer et al., 2015; Majka et al., 2012; Svenningsen, 2000) are shown by the horizontal dashed line and horizontal gray bar, respectively.

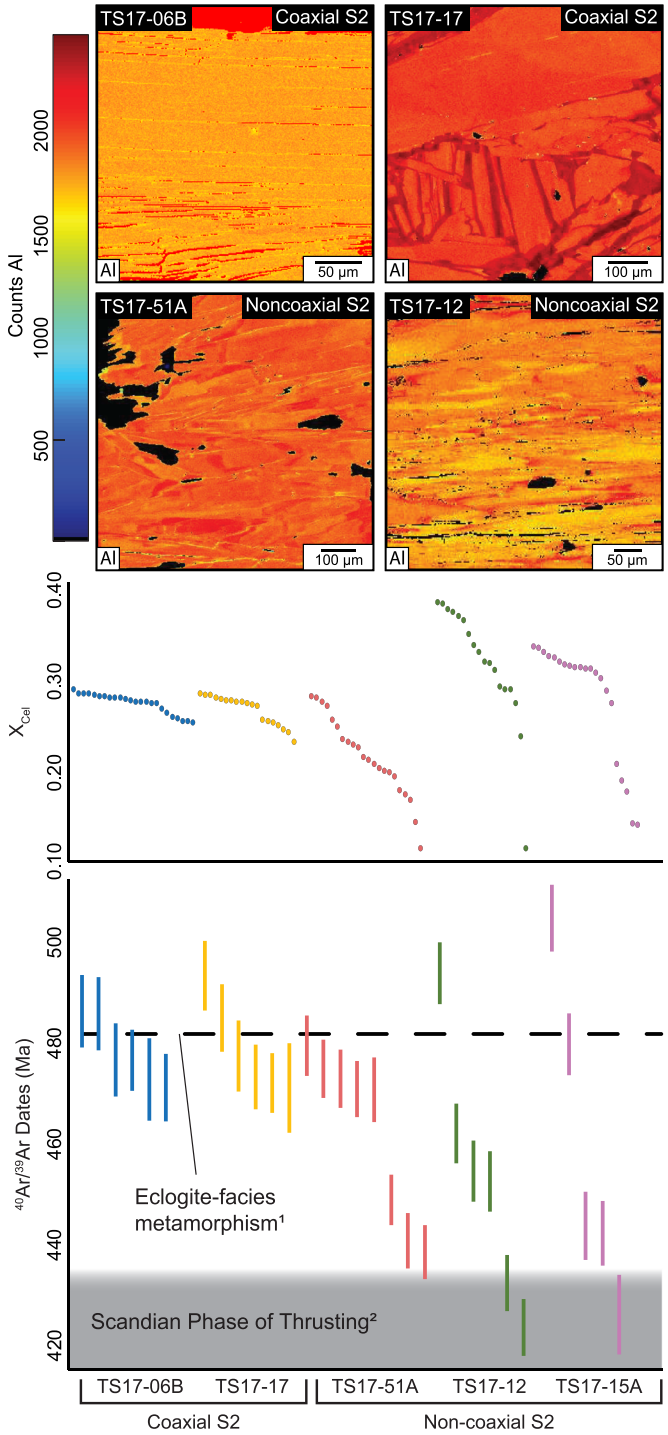

Figure 7. Qualitative electron microprobe X-ray chemical maps of Al (top) and quantitative wavelength-dispersive spectroscopy geochemical results (X_{Cel}) with $^{40}Ar/^{39}Ar$ dates (bottom) for samples containing S2. The chemical maps were used for dating and depict white micas that were analyzed for $^{40}Ar/^{39}Ar$ geochronology. Two representative maps are presented for samples containing coaxial S2 and noncoaxial S2. Minerals other than white mica in the maps were masked using XMapTools v. 2.6.4 (Lanari et al., 2014). The individual $^{40}Ar/^{39}Ar$ dates ($\pm 1\sigma$ uncertainties) are plotted for each sample below the quantitative geochemical data. The samples are classified according to their microstructures. The timing of eclogite facies metamorphism [1](Root & Corfu, 2012) and the timing of Scandian thrusting [2](Andréasson et al., 2018; Bender et al., 2019; Dallmeyer, 1990; Dallmeyer & Gee, 1988; Grimmer et al., 2015; Majka et al., 2012; Svenningsen, 2000) are shown by the horizontal dashed line and horizontal gray bar, respectively.

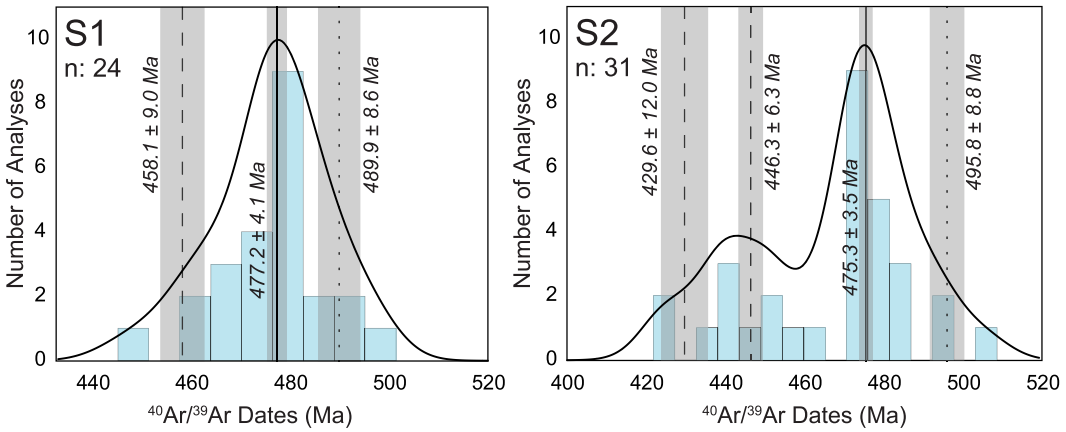

Figure 8. Histograms (blue bars), cumulative Gaussian curve plot (curved black lines), and Gaussian deconvolution ages of the ^{40}Ar/^{39}Ar dates for samples containing S1 (left) and S2 (right) microstructures. The reported age populations (two uncertainties) are represented by the vertical gray bars. Age populations are interpreted to represent extraneous ^{40}Ar (dotted lines), cooling age of the Tsäkkok Lens (solid lines) or (partial) resetting of the cooling record due to recrystallization/neocrystallization via deformation (dashed lines).

Twenty-four analyses were performed on white micas that define S1 (Figure 6) in Samples TS17-15B (undeformed S1) and TS17-27, TS17-30, and TS17-33B (S1 folded by F2). Thirty-one analyses were also conducted on white mica-defining S2 (Figure 7) in Samples TS17-06B, TS17-12, TS17-15A, TS17-17, and TS17-51A. The collective results of the four samples of S1 provided a range of dates from 496.0 ± 5.8 to 448.3 ± 6.6 Ma (1σ). Two of the samples (TS17-15B and TS17-33B) show ^{40}Ar/^{39}Ar dates grouped between 496.0 ± 5.8 and 469.2 ± 7.3 Ma (n = 12), whereas the other two samples (TS17-27 and TS17-30) are more scattered from 493.7 ± 7.0 to 448.3 ± 6.6 Ma (n = 12). The results of the analyses performed on the five samples of S2 yield dates from 505.0 ± 6.6 to 423.8 ± 5.7 Ma (1σ). Two of the samples are defined by coaxial structures (TS17-06B and TS17-17) and yielded dates between 493.6 ± 6.9 and 471.3 ± 8.9 Ma (n = 12). Three of the samples contained noncoaxial structures. Of these, two (TS17-12 and TS17-15A) provide a range of dates from 505.0 ± 6.6 to 423.8 ± 5.7 Ma (n = 11) and the third sample (TS17-51A) shows a bimodal distribution of 479.7 ± 6.0 to 470.9 ± 6.4 Ma (n = 5), and 449.1 ± 5.0 to 438.7 ± 5.4 Ma (n = 3).

Due to the distribution of dates, the collective data sets for S1- and S2-bearing samples was further evaluated using the Gaussian deconvolution function in Isoplot v.4.15 (Ludwig, 2012; Figure 8). The methodology for evaluating potential populations was adopted from Sambridge and Compston (1994). The uncertainties of the populations were assessed following the approach in Barnes et al. (2020), and it was determined that the uncertainties assigned by the Gaussian deconvolution evaluation account for both of the reported uncertainty of each ^{40}Ar/^{39}Ar date, and the scatter of the data set. The resulting populations (±2σ uncertainties) for the S1 samples are 489.8 ± 8.6, 477.2 ± 4.1, and 458.1 ± 9.0 Ma (Figure 8). The samples of S2 yield populations of 495.8 ± 8.8, 475.3 ± 3.5, 446.3 ± 6.3, and 429.6 ± 12.0 Ma (Figure 8). To confirm that the method of grouping samples defined by S1 versus S2 did not bias the results, the Gaussian deconvolution was also applied to the collective dates of all nine samples, as well as the multiple grouping based on further subdivision of structures (i.e., grouped S1, S1 folded by F2, coaxial S2, and noncoaxial S2). Both of the approaches provide comparable results to the results reported above (supporting information Text S2). Therefore, the different populations are not controlled by the statistical evaluation of the structural groupings but rather by ^{40}Ar diffusion reflecting the conditions in which the dated structures formed.

5. Discussion

5.1. Deformation History

Three phases of deformation in the Tsäkkok Lens have been identified that record the subduction to exhumation cycle during the Caledonian Orogeny. The D1 event is interpreted to record prograde to peak metamorphism of the Tsäkkok Lens. The D2 event, which is pervasive throughout the Tsäkkok Lens, provides the record of exhumation. The early D2 structures represent coaxial strain and vertical shortening. D2

predominantly occurred within amphibolite-facies to perhaps greenschist-facies conditions. This is evinced by the amphibolitized margins of eclogite bodies that are concordant with the surrounding S2. On the microscale, retrogression of monazite to apatite, allanite, and clinozoisite coronas aligned with S2 is typical for amphibole- to greenschist-facies conditions (Janots et al., 2007; Kośmińska et al., 2020; Spear, 2010), which is also supported by retrogression of garnet to chlorite. Temperatures of deformation can be semiquantitatively constrained by the crystal plastic deformation of plagioclase (i.e., undulatory extinction and subgrain rotation recrystallization) observed in multiple samples (i.e., TS17-06B, TS17-12, TS17-27, and TS17-30). These deformation mechanisms have been determined to operate at temperatures of 450°C and higher (Rosenberg & Stünitz, 2003; Rybacki & Dresen, 2000; Wintsch & Yi, 2002), supporting the mesoscale and microscale observations for amphibolite-facies conditions of D2.

Textural relationships indicate that coaxial deformation was overprinted by noncoaxial deformation (i.e., anastomosing shear bands overprinting the relatively undeformed S2 in TS17-06B and TS17-12) that shows a general top to east sense of shear. The noncoaxial stage of deformation is interpreted to reflect Scandian thrusting that is responsible for foreland-directed nappe emplacement (Figures 1 and 2). Scandian thrusting occurred in response to continental collision recorded from circa 435 Ma (Andréasson et al., 2018; Bender et al., 2019; Dallmeyer, 1990; Dallmeyer & Gee, 1988; Grimmer et al., 2015; Majka et al., 2012; Svenningsen, 2000). Provided that the foliation of the Scandian thrust is concordant with S2, we postulate that Scandian thrusting demarcates the final stage of D2 deformation in the Tsäkkok Lens. Phyllonites and plastically deformed calcite marbles in the Scandian thrust zone indicate that deformation occurred in a minimum of greenschist-facies conditions (Busch & van der Pluijm, 1995; Rutter, 1976; Vernon, 1981). Altogether, the entire set of D2 structures and associated paragenetic assemblages show that D2 deformation operated during retrogression from eclogite-facies conditions (>14 kbar and ~630°C; Kullerud, 1987; Stephens & van Roermund, 1984) to greenschist-facies conditions.

The D3 event comprises broad-scale open folds (F3) that refolded F2 and reoriented both S1 and S2 (Figures 2 and 9). Overall, this event produced NE-SW directed shortening. The KNC was folded together with the Tsäkkok Lens, indicating that NE-SW shortening during D3 deformation occurred after Scandian thrusting in upper crustal conditions. However, the P-T conditions cannot be constrained as no foliation mineral paragenesis nor microstructures associated with D3 have been recognized. The relative timing of folding (i.e., after Scandian thrusting) is also recognized in the Staloluokta Window (Stølen, 1988), northwest of the field area (Figure 1), and in the Bångonåive and Fjällfjället windows (Stephens, 1977, 1982; Zachrisson, 1969), ~200–275 km further to the southwest in Västerbotten.

5.2. Postdecompression Cooling of the Tsäkkok Lens

Both samples of S1 and S2 structures investigated in this study yield $^{40}Ar/^{39}Ar$ populations that are slightly older (489.8 ± 8.6 and 495.8 ± 8.8 Ma) and slightly younger (477.2 ± 4.1 and 475.3 ± 3.5 Ma) than the timing of eclogite-facies metamorphism (481.9 ± 1.2 Ma; Root & Corfu, 2012). The P-T estimates for these rocks of ~22 kbar and ~590°C (Bukała et al., 2020) for eclogite-facies conditions should have been conducive for thermal diffusion of ^{40}Ar out of the mica (Harrison et al., 2009; Warren, Hanke, & Kelley, 2012). Additionally, overprinting of S1 by D2 structures would have provided a means to obscure a previous $^{40}Ar/^{39}Ar$ record. However, the existence of these few, older dates likely suggests the presence of extraneous ^{40}Ar in both S1- and S2-defining white micas. This is possibly due to incomplete degassing of $^{40}Ar^*$ or the incorporation of excess ^{40}Ar during recrystallization/neocrystallization of the white micas coinciding with transposition of S1 into S2 (McDonald et al., 2018; Warren et al., 2011, 2012). Unfortunately, an inverse isochron of this oldest data set does not reveal any additional information due to the tight clustering of highly radiogenic data.

The second oldest populations of 477.2 ± 4.1 and 475.3 ± 3.5 Ma (S1 and S2, respectively) originate from eight of the nine samples. However, this record is best preserved in four samples that do not yield dates younger than circa 469 Ma: the undeformed S1 (TS17-15B), S1 that is folded by F2 with plagioclase porphyroblasts overgrowing the folds (TS17-33B), and two S2 samples with coaxial structures (TS17-06B and TS17-17). The variety of these structures demonstrates that there is no correlation between (micro)structures and the $^{40}Ar/^{39}Ar$ dates in these rocks. These four samples also exhibit homogeneous mica chemistry that correlates well with the relatively uniform distribution of $^{40}Ar/^{39}Ar$ dates. The homogeneity of major elements suggests that the sequence of structures formed in temperature conditions that were suitable for

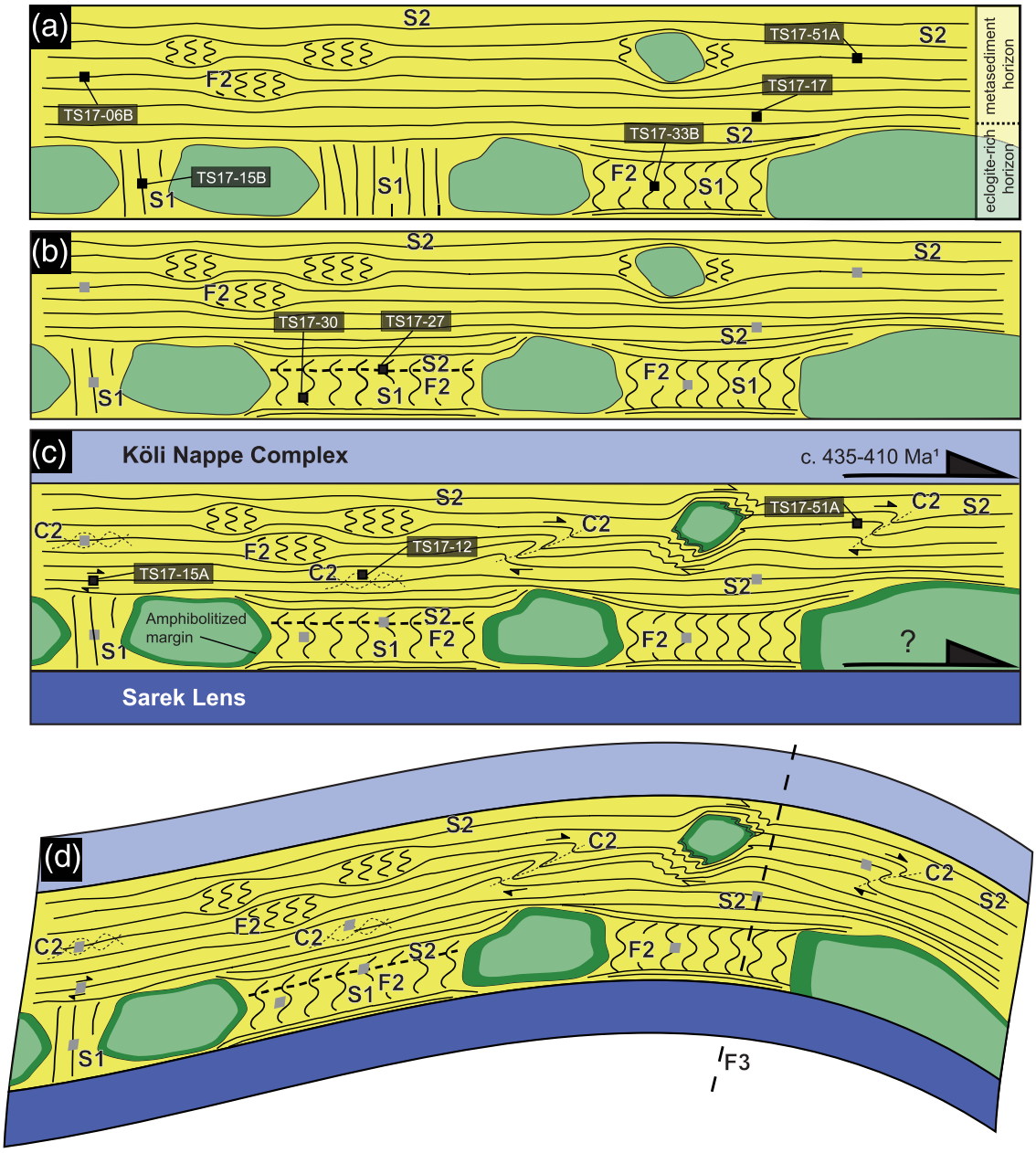

Figure 9. Schematic representation of the structural and temporal evolution for the Tsäkkok Lens during exhumation from eclogite-facies conditions. (a) Vertical shortening during the incipient stages of D2 defined by F2 folding of S1 and development of S2. This stage of D2 is predominantly characterized by coaxial strain. S1 is best preserved proximal to the eclogite bodies. The marked samples yield $^{40}Ar/^{39}Ar$ white mica ages that record exhumation and cooling through the white mica ^{40}Ar closure temperature in the Tsäkkok Lens at 477.2 ± 4.1 Ma (S1) or 475.3 ± 3.5 Ma (S2). b) Protracted vertical shortening of the Tsäkkok Lens recorded by late-stage F2 of the S1 in eclogite-rich horizons. The $^{40}Ar/^{39}Ar$ dates for these folded samples exhibit partial resetting suggesting that localized F2 folding occurred in pressure and temperature conditions that were too low for thermally activated diffusion of ^{40}Ar. The timing of late-stage F2 is tentatively resolved to 458.1 ± 9.0 Ma. (c) Noncoaxial deformation represented by C2 shear zones, associated drag folding of S2, possible quarter structures around rigid eclogite bodies and anastomosing μm-scale shear bands that disrupt S2. The timing of noncoaxial deformation is resolved to 429.6 ± 12.0 Ma, which corresponds to the timing of overthrusting of the Köli Nappe complex. The marked samples yield $^{40}Ar/^{39}Ar$ white mica ages that record possible partial to total resetting of the cooling ages, as a result of recrystallization/neocrystallization of the white micas via noncoaxial D2 deformation. [1](Andréasson et al., 2018; Bender et al., 2019; Dallmeyer, 1990; Dallmeyer & Gee, 1988; Grimmer et al., 2015; Majka et al., 2012; Svenningsen, 2000). The timing of overthrusting of the Sarek Lens by the Tsäkkok Lens is not resolved. (d) The D3 stage is represented by shallow crustal km- to m-scale F3 folding of the Tsäkkok Lens, together with the overlying Köli Nappe complex and the underlying Sarek Lens. The km-scale F3 folds control the bulk architecture of the Tsäkkok Lens and reoriented both the D1 and D2 structures.

reequilibration of major elements, which has previously been estimated to occur at >500°C (Dempster, 1992; Giorgis et al., 2000).

The lack of structural correlation, in combination with temperature estimates for retrogressive metamorphism, deformation, and chemical equilibration during early D2, suggests that the circa 477- to 475-Ma populations record closure of ^{40}Ar diffusion during cooling of the Tsäkkok Lens. However, the exhumation pathway of the Tsäkkok Lens is initially defined by nearly isothermal decompression, subsequently followed by nearly isobaric cooling (Kullerud, 1987). Decompression is proposed to decrease retentivity of ^{40}Ar in white mica (Harrison et al., 2009; Warren, Hanke, & Kelley, 2012) indicating that the circa 477- to 475-Ma populations should not record the initial decompression history but instead record the nearly isobaric cooling segment of the P-T pathway. Based on the estimated pressure of isobaric cooling (Kullerud, 1987), and the various parameters outlined in Warren, Hanke, and Kelley (2012), the argon closure temperature is suggested to be in the range of 400–500°C, slightly cooler than the estimated temperatures for early D2. This reaffirms that the coaxial structures related to early D2 formed along the decompression pathway prior to cooling.

5.3. Partial Resetting of the Cooling Record Due to Deformation

Five samples provide a scatter of ^{40}Ar/^{39}Ar dates. Two samples containing S1 folded by F2 (TS17-27 and TS17-30) preserve ^{40}Ar/^{39}Ar dates that contributed to the circa 477- to 475-Ma age population and also contain younger dates that define a population at 458.1 ± 9.0 Ma. The three samples containing S2 and noncoaxial structures also document cooling but are dominated by a younger dispersion of dates that define populations of 446.3 ± 6.3 and 429.6 ± 12.0 Ma. Dispersed ^{40}Ar/^{39}Ar dates may be the result of the incorporation of extraneous ^{40}Ar (Giorgis et al., 2000; Uunk et al., 2018), retrogressive reactions causing partial ^{40}Ar* loss and resetting of ^{40}Ar/^{39}Ar dates (Allaz et al., 2011), or incomplete removal of ^{40}Ar from the grain via, for example, recrystallization during deformation (Cossette et al., 2015; Kellett et al., 2016; Kramar et al., 2001; Mulch & Cosca, 2004; Uunk et al., 2018). As these samples yield dates that are younger than the dominant record of cooling (section 5.2), the presence of extraneous ^{40}Ar is not a likely option. We do not interpret that the effects of retrogressive reactions are the cause of partial ^{40}Ar loss as our dating methodology endeavored avoid any effects of retrogressive replacement of white mica by biotite or chlorite. Instead, we interpret the microstructural evidence recorded within the Tsäkkok Lens metasediments to support partial ^{40}Ar loss during the later stages of D2. The white mica-defining D2 structures in these samples also show dispersion in the endmember compositions, indicating that the conditions for deformation were too low to allow for reequilibration of major elements in the white micas during noncoaxial deformation (Dempster, 1992; Giorgis et al., 2000). Decreasing pressure conditions is suggested by the lower X_{Cel} values from values of the noncoaxial samples, compared to the coaxially deformed D1 and D2 samples.

The F2 folding of S1 is best preserved in areas that have abundant eclogite bodies. The localized preservation of these structures was likely controlled by the spatial distribution of rigid eclogite bodies that protected adjacent S1 from transposition into S2 (Figure 3c). However, a noncontemporaneous history of F2 is evident from samples of the same structural classification provide different ^{40}Ar/^{39}Ar records (i.e., TS17-33B vs. TS17-27 and TS17-30). The noncontemporaneous F2 history is supported by the observed microstructures in plagioclase porphyroblasts (Figures 5a–5c). White mica inclusions in plagioclase porphyroblasts that overgrew D2 structures (i.e., TS17-12 and TS17-33B) suggest that plagioclase grew during decompression from HP conditions and thus can be compared relative to the timing of deformation events. Based on the textural relationships of S1 and S2, and white mica inclusions in plagioclase, the porphyroblasts either overgrew F2 (TS17-33B; Figure 5a) or crystallized prior to F2 (TS17-27 and TS17-30; Figures 5b and 5c). The plagioclase in the latter case is highly strained, exhibiting strong evidence for (sub)grain boundary development. Such microstructures indicate temperatures during deformation were >450°C (Rosenberg & Stünitz, 2003). The circa 458-Ma population produced by the two partially reset samples indicates that vertical shortening continued in the Tsäkkok Lens until that time, or later.

For the three noncoaxially deformed samples, it is difficult to ascribe geological meaning to the circa 446-Ma population as they represent partial resetting of the older cooling history. However, the circa 430-Ma population is in agreement with the general timing of Scandian thrusting from circa 435 Ma (Andréasson et al., 2018; Bender et al., 2019; Dallmeyer, 1990; Dallmeyer & Gee, 1988; Grimmer et al., 2015;

Majka et al., 2012; Svenningsen, 2000). The circa 430-Ma population is therefore interpreted as a maximum age for Scandian deformation that penetrated the Tsäkkok Lens.

5.4. Possible Exhumation Mechanisms for the Tsäkkok Lens

The results of this study provide a detailed structural and geochronological evolution of the Tsäkkok Lens during exhumation from eclogite-facies conditions (Figure 9). Although based on few samples, it is suggested that initial decompression is characterized by vertical shortening and coaxial deformation, a phenomenon for HP localities in the well-studied Western Gneiss Region (Andersen et al., 1994; Engvik & Andersen, 2000; Foreman et al., 2005; Krabbendam & Wain, 1997). The $^{40}Ar/^{39}Ar$ dates record the timing of nearly isobaric cooling (477.2 ± 4.1 to 475.3 ± 3.5 Ma) after decompression from eclogite-facies conditions (Figure 8). The pressure recorded for S2 development is as shallow as 6 kbar (Snilsberg, 1987). This suggests that the rocks of the Tsäkkok Lens exhumed to midcrustal depths from eclogite-facies conditions in ~5–7 Myr It is also plausible that the Tsäkkok Lens rocks reached shallower levels before the Silurian, which are not recorded by S2. Surface exposure of HP rocks in the Silurian is readily observed in the Høyvik Group in southwestern Norway (Andersen et al., 1998; Brekke & Solberg, 1987), as well as the Vestgötabreen Complex in western Svalbard (Armstrong et al., 1986; Ohta et al., 1983). For the latter locality, cooling at 476 ± 2 Ma indicates that exhumation was coeval with the Tsäkkok Lens (Barnes et al., 2020).

Peak pressures for the Tsäkkok Lens have recently been resolved to ~22 kbar (Bukała et al., 2020). Although overpressures of up to 20% have been modeled for subducting rocks (Burg & Gerya, 2005; Li et al., 2010), we approximate the maximum exhumation rate for the Tsäkkok Lens by assuming no overpressure through the peak and exhumation stages (e.g., Burov & Yamato, 2008) and that the lens cooled in shallow-crustal conditions ~5 Myr after peak conditions. This results in an average exhumation rate up to ~1.2 cm/yr before cooling, which is well within the rates of exhumation for other UHP localities worldwide. For example, the UHP Dora Maira rocks record exhumation rates up to 3.4 cm/yr, assuming that the rocks were not overpressured (Rubatto & Hermann, 2001). Exhumation at such rates is promoted by buoyancy of the subducted crustal rock, which is effective until midcrustal depths (e.g., Baldwin et al., 2004; Carswell et al., 2003; Ernst, 2001; Ernst et al., 1997; Glodny et al., 2005; Hacker, 2007; Parrish et al., 2006; Rubatto & Hermann, 2001; Smye et al., 2011; Terry et al., 2000). Indeed, the Tsäkkok Lens is dominated by siliciclastic and carbonaceous metasedimentary rocks, providing an overall buoyant rock assemblage. The short-duration (<10 Myr) for exhumation of the Tsäkkok Lens suggests exhumation during active subduction rather than reversal of the subduction zone (e.g., Warren, 2013) prior to continental collision. This is in direct contrast to the slower exhumation of the much larger Western Gneiss Region (e.g., Hacker & Gerya, 2013; Kylander-Clark et al., 2012; Warren, 2013) that possibly occurred due to eduction of the lower plate during continental collision (Andersen et al., 1991; Bottrill et al., 2014; Butler et al., 2015). Therefore, while the Tsäkkok Lens and the rocks of the Western Gneiss Region may share some similarities, they require different tectonic regimes to explain their exhumation histories. The HP Tsäkkok Lens may have been exhumed due to divergent motions of the lower plate (e.g., slab-rollback; Brun & Faccenna, 2008) or by upper plate divergence from the lower plate (e.g., Froitzheim et al., 2003; Liao et al., 2018; Majka et al., 2014). Such mechanisms may be applicable for the Tsäkkok Lens but require a more regional investigation to determine a best fit model.

Noncoaxial D2 associated with subsequent Scandian collision penetrated the Tsäkkok Lens and overprinted the older S2 coaxial fabrics. Tectonic burial is implied by overthrusting of the KNC. Although the data set presented here does not confirm such tectonics, postcollisional exhumation of the SNC in Norrbotten would require significant erosion and possibly extensional faulting during or after tectonic burial. Models suggest that postcollisional extensional faulting was responsible for unroofing the HP rocks, which is well documented in the southwestern Scandinavian Caledonides, particularly for the Western Gneiss Region (e.g., Andersen et al., 1991; Fossen, 2010; Hacker et al., 2010). Extensional faults have not been directly described for southern Norrbotten, but they are recognized ~100–150 km to the north in the Ofoten-Troms region (Coker et al., 1995; Fossen & Rykkelid, 1992). Additionally, the F3 folding of the KNC-SNC package exhibits similar style and vergence as those documented in the Western Gneiss Region, which has been described as the latest stage for postcollisional exhumation (Chauvet & Séranne, 1994). Therefore, the extensional faulting in regions proximal to the Tsäkkok Lens, and postcollisional F3 folding of the SNC suggests that the latest stage of exhumation followed a similar tectonic evolution as in the Western Gneiss Region.

6. Conclusions

The history of subduction and subsequent exhumation to shallow crustal levels can be distinguished by three distinct deformation events. D1 is preserved as a relic S1, which is locally folded by F2 and transposed by S2 that together defines the second event, D2. The second deformation stage is associated with vertical shortening and subsequent broad top to east sense of shear. Overall, D2 represents exhumation of the Tsäkkok Lens from eclogite-facies conditions in the Early Ordovician to greenschist-facies during Scandian thrusting due to continental collision between Laurentia and Baltica in the Silurian. Results of $^{40}Ar/^{39}Ar$ geochronological analysis of white micas-defining D1 structures and coaxial D2 structures record cooling (477.2 ± 4.1 to 475.3 ± 3.5 Ma) after rapid, nearly isothermal decompression of the Tsäkkok Lens. Postcooling F2 folding suggests that vertical shortening may have occurred (tentatively until 458.1 ± 9.0 Ma). Late-stage noncoaxial D2 locally reworked some of the previous structures and record deformation that penetrated the Tsäkkok Lens during Scandian thrusting (429.6 ± 12.0 Ma), which (partially) reset the previous record of cooling. Increased heterogeneity of the white mica chemistry is positively correlated with resetting of the $^{40}Ar/^{39}Ar$ dates. Final exhumation of the Tsäkkok Lens was likely governed by post-Scandian extensional faulting and erosion. The D3 event that is manifested as F3 folding resulted in NE-SW shortening of the KNC-SNC assembly and may reflect the final stage of exhumation.

Data Availability Statement

Data for geochemical and geochronological analyses that were used for the figures and interpretations are being reviewed for submission to the 4TU.Centre for Research Data repository to be in compliance with FAIR Data standards and has been issued DOI (10.4121/uuid:fccd7c19-ec6f-438a-876c-bcab3b59b221).

Acknowledgments

This study was funded by the National Science Centre, Poland (CALSUB Project 2014/14/E/ST10/00321). Other financial support has been provided by the Polish National Agency for Academic Exchange Scholarship PPN/IWA/2018/1/00030/U/00001 (C. Barnes). We would like to thank Adam Włodek (AGH University of Science and Technology) for his assistance on the electron microprobe, as well as Alfredo Camacho for his assistance with in situ $^{40}Ar/^{39}Ar$ geochronology. We are grateful to Laurent Jolivet for his editorial handling and comments. The comments provided by Federico Rossetti, Jo-Anne Wartho, and Torgeir B. Andersen are very much appreciated for the improvement of this article.

References

Allaz, J., Engi, M., Berger, A., & Villa, I. M. (2011). The effects of retrograde reactions and of diffusion on ^{40}Ar-^{39}Ar ages of micas. *Journal of Petrology*, *52*(4), 691–716. https://doi.org/10.1093/petrology/egq100

Andersen, T. B., Berry, H. N. IV, Lux, D. R., & Andresen, A. (1998). The tectonic significance of pre-Scandian $^{40}Ar/^{39}Ar$ phengite cooling ages in the Caledonides of western Norway. *Journal of the Geological Society*, *155*(2), 297–309. https://doi.org/10.1144/gsjgs.155.2.0297

Andersen, T. B., Jamtveit, B., Dewey, J. F., & Swensson, E. (1991). Subduction and eduction of continental crust: Major mechanisms during continent-continent collision and orogenic extensional collapse, a model based on the south Norwegian Caledonides. *Terra Nova*, *3*(3), 303–310. https://doi.org/10.1111/j.1365-3121.1991.tb00148.x

Andersen, T. B., Osmundsen, P. T., & Jolivet, L. (1994). Deep crustal fabrics and a model for the extensional collapse of the southwest Norwegian Caledonides. *Journal of Structural Geology*, *16*(9), 1191–1203. https://doi.org/10.1016/0191-8141(94)90063-9

Andréasson, P.-G. (1987). Early evolution of the late Proterozoic Baltoscandian margin. *Geologiska Föreningen i Stockholm Förhandlingar*, *109*(4), 336–340. https://doi.org/10.1080/11035898709453101

Andréasson, P.-G., Allen, A., Aurell, O., Boman, D., Ekestubbe, J., Goerke, U., et al. (2018). Seve terranes of the Kebnekaise Mts., Swedish Caledonides, and their amalgamation, accretion and affinity. *GFF*, *144*, 1–28. https://doi.org/10.1080/11035897.2018.1470200

Andréasson, P.-G., & Gee, D. G. (1988). Thrusting along the Baltoscandian margin related to early Caledonian (Finnmarkian) subduction. *Geologiska Föreningen i Stockholm Förhandlingar*, *110*(4), 378–379. https://doi.org/10.1080/11035898809452674

Andréasson, P.-G., Svenningsen, O., Johansson, I., Solyom, Z., & Xiaodan, T. (1992). Mafic dyke swarms of the Baltica-Iapetus transition, Seve Nappe complex of the Sarek Mts., Swedish Caledonides. *Geologiska Föreningen i Stockholm Förhandlingar*, *114*(1), 31–45. https://doi.org/10.1080/11035899209453460

Armstrong, H. A., Nakrem, H. A., & Ohta, Y. (1986). Ordovician conodonts from the Bulltinden formation, Motalafjella, Central-Western Spitsbergen. *Polar Research*, *4*(1), 17–23. https://doi.org/10.1111/j.1751-8369.1986.tb00514.x

Baldwin, S. L., Monteleone, B. B., Webb, L. E., Fitzgerald, P. G., Grove, M., & Hill, E. J. (2004). Pliocene eclogite exhumation at plate tectonic rates in eastern Papua New Guinea. *Nature*, *431*(7006), 263–267. https://doi.org/10.1038/nature02846

Barnes, C. J., Walczak, K., Janots, E., Schneider, D., & Majka, J. (2020). Timing of paleozoic exhumation and deformation of the high-pressure vestg□tabreen complex at the Motalafjella Nunatak, Svalbard. *Minerals*, *10*(2), 125. https://doi.org/10.3390/min10020125

Bender, H., Glodny, J., & Ring, U. (2019). Absolute timing of Caledonian orogenic wedge assembly, Central Sweden, constrained by Rb-Sr multi-mineral isochron data. *Lithos*, *344-345*, 339–359. https://doi.org/10.1016/j.lithos.2019.06.033

Bottrill, A. D., van Hunen, J., Cuthbert, S. J., Brueckner, H. K., & Allen, M. B. (2014). Plate rotation during continental collision and its relationship with the exhumation of UHP metamorphic terranes: Application to the Norwegian Caledonides. *Geochemistry, Geophysics, Geosystems*, *15*, 1766–1782. https://doi.org/10.1002/2014GC005253.Received

Brekke, H., & Solberg, P. O. (1987). The geology of Atløy, Sunnfjord, western Norway. *Norges Geologiske Undersøkelse Bulletin*, *410*, 73–49.

Brueckner, H. K., & van Roermund, H. L. M. (2004). Dunk tectonics: A multiple subduction/eduction model for the evolution of the Scandinavian Caledonides. *Tectonics*, *23*, TC2004. https://doi.org/10.1029/2003TC001502

Brun, J.-P., & Faccenna, C. (2008). Exhumation of high-pressure rocks driven by slab rollback. *Earth and Planetary Science Letters*, *272*(1-2), 1–7. https://doi.org/10.1016/j.epsl.2008.02.038

Bukała, M., Klonowska, I., Barnes, C., Majka, J., Kośmińska, K., Janák, M., et al. (2018). UHP metamorphism recorded by phengite eclogite from the Caledonides of northern Sweden: P–T path and tectonic implications. *Journal of Metamorphic Geology*, *36*(5), 547–566. https://doi.org/10.1111/jmg.12306

Bukała, M. B., Hidas, K., Garrido, C. J., Barnes, C., Klonowska, I., & Majka, J. (2020) *Deciphering the brittle failure of eclogites at high-pressures: Hydrofractures as fluid-escape pathways*. Vienna, Austria: EGU General Assembly.

Burg, J. P., & Gerya, T. V. (2005). The role of viscous heating in Barrovian metamorphism of collisional orogens: Thermomechanical models and application to the Lepontine dome in the Central Alps. *Journal of Metamorphic Geology*, *23*(2), 75–95. https://doi.org/10.1111/j.1525-1314.2005.00563.x

Burov, E., & Yamato, P. (2008). Continental plate collision, P-T-t-z conditions and unstable vs. stable plate dynamics: Insights from thermo-mechanical modelling. *Lithos*, *103*(1–2), 178–204. https://doi.org/10.1016/j.lithos.2007.09.014

Busch, J. P., & van Der Pluijm, B. A. (1995). Calcite textures, microstructures and rheological properties of marble mylonites in the Bancroft shear zone, Ontario, Canada. *Journal of Structural Geology*, *17*(5), 677–688. https://doi.org/10.1016/0191-8141(94)00092-E

Butler, J. P., Beaumont, C., & Jamieson, R. A. (2015). Paradigm lost: Buoyancy thwarted by the strength of the western gneiss region (ultra) high-pressure terrane, Norway. *Lithosphere*, *7*(4), 379–407. https://doi.org/10.1130/L426.1

Carswell, D. A., Brueckner, H. K., Cuthbert, S. J., Mehta, K., & O'Brien, P. J. (2003). The timing of stabilisation and the exhumation rate for ultra-high pressure rocks in the Western gneiss region of Norway. *Journal of Metamorphic Geology*, *21*(6), 601–612. https://doi.org/10.1046/j.1525-1314.2003.00467.x

Chauvet, A., & Séranne, M. (1994). Extension-parallel folding in the Scandinavian Caledonides: Implications for late-orogenic processes. *Tectonophysics*, *238*(1–4), 31–54. https://doi.org/10.1016/0040-1951(94)90048-5

Chemenda, A. I., Mattauer, M., Malavieille, J., & Bokun, A. N. (1995). A mechanism for syn-collisional rock exhumation and associated normal faulting: Results from physical modelling. *Earth and Planetary Science Letters*, *132*(1-4), 225–232. https://doi.org/10.1016/0012-821X(95)00042-B

Chopin, C. (1984). Coesite and pure pyrope in high-grade blueschists of the Western Alps: A first record and some consequences. *Contributions to Mineralogy and Petrology*, *86*(2), 107–118. https://doi.org/10.1007/BF00381838

Chopin, C. (2003). Ultrahigh-pressure metamorphism: Tracing continental crust into the mantle. *Earth and Planetary Science Letters*, *212*(1-2), 1–14. https://doi.org/10.1016/S0012-821X(03)00261-9

Coggon, R., & Holland, T. J. B. (2002). Mixing properties of phengitic micas and revised garnet-phengite thermobarometers. *Journal of Metamorphic Geology*, *20*(7), 683–696. https://doi.org/10.1046/j.1525-1314.2002.00395.x

Coker, J. E., Steltenpohl, M. G., Andresen, A., & Kunk, M. J. (1995). An $^{40}Ar/^{39}Ar$ thermochronology of the Ofoten-Troms region: Implications for terrane amalgamation and extensional collapse of the northern Scandinavian Caledonides. *Tectonics*, *14*(2), 435–447. https://doi.org/10.1029/94TC03091

Corfu, F., Andersen, T. B., & Gasser, D. (2014). The Scandinavian Caledonides: Main features, conceptual advances and critical questions. In F. Corfu, D. Gasser, & D. M. Chew (Eds.), *New Perspectives on the Caledonides of Scandinavia and Related Areas* (Vol. 390, pp. 9, 1–43). London, England: Geological Society London, Special Publications. https://doi.org/10.1144/SP390.25

Cosca, M., Stunitz, H., Bourgeix, A.-L., & Lee, J. P. (2011). $^{40}Ar^*$ loss in experimentally deformed muscovite and biotite with implications for $^{40}Ar/^{39}Ar$ geochronology of naturally deformed rocks. *Geochimica et Cosmochimica Acta*, *75*(24), 7759–7778. https://doi.org/10.1016/j.gca.2011.10.012

Cossette, É., Schneider, D. A., Warren, C. J., & Grasemann, B. (2015). Lithological, rheological, and fluid infiltration control on $^{40}Ar/^{39}Ar$ ages in polydeformed rocks from the west Cycladic detachment system, Greece. *Lithosphere*, *7*(2), 189–205. https://doi.org/10.1130/L416.1

Dallmeyer, R. D. (1990). $^{40}Ar/^{39}Ar$ mineral age record of a polyorogenic evolution within the Seve and Köli nappes, Trøndelag, Norway. *Tectonophysics*, *179*(3-4), 199–226. https://doi.org/10.1016/0040-1951(90)90291-F

Dallmeyer, R. D., & Gee, D. G. (1988). Polyorogenic $^{40}Ar/^{39}Ar$ mineral age record in the Seve and Köli Nappes of the Gäddede area, northwestern Jämtland, central Scandinavian Caledonides. *Journal of Geology*, *96*(2), 181–198. https://doi.org/10.1086/629208

Dallmeyer, R. D., & Stephens, M. B. (1991). Chronology of eclogite retrogression within the Seve Nappe complex, Råvvejaure, Sweden: Evidence from $^{40}Ar/^{39}Ar$ mineral ages. *Geologische Runschau*, *80*(3), 729–743. https://doi.org/10.1007/BF01803698

Dempster, T. J. (1992). Zoning and recrystallization of phengitic micas: Implications for metamorphic equilibration. *Contributions to Mineralogy and Petrology*, *109*(4), 526–537. https://doi.org/10.1007/BF00306554

Egli, D., Mancktelow, N., & Spikings, R. (2017). Constraints from $^{40}Ar/^{39}Ar$ geochronology on the timing of alpine shear zones in the mont blanc-aiguilles rouges region of the European alps. *Tectonics*, *36*, 730–748. https://doi.org/10.1002/2016TC004450

Engvik, A. K., & Andersen, T. B. (2000). Evolution of Caledonian deformation fabrics under eclogite and amphibolite facies at Vardalsneset, Western gneiss region, Norway. *Journal of Metamorphic Geology*, *18*(3), 241–257. https://doi.org/10.1046/j.1525-1314.2000.00252.x

Ernst, W. G. (2001). Subduction, ultrahigh-pressure metamorphism, and regurgitation of buoyant crustal slices—Implications for arcs and continental growth. *Physics of the Earth and Planetary Interiors*, *127*(1-4), 253–275. https://doi.org/10.1016/S0031-9201(01)00231-X

Ernst, W. G., Maruyama, S., & Wallis, S. (1997). Buoyancy-driven, rapid exhumation of ultrahigh-pressure metamorphosed continental crust. *Proceedings of the National Academy of Sciences of the United States of America*, *94*, 9532–9537. https://doi.org/10.1073/pnas.94.18.9532

Foreman, R., Andersen, T. B., & Wheeler, J. (2005). Eclogite-facies polyphase deformation of the Drøsdal eclogite, Western gneiss complex, Norway, and implications for exhumation. *Tectonophysics*, *398*(1–2), 1–32. https://doi.org/10.1016/j.tecto.2004.10.003

Fossen, H. (2010). Extensional tectonics in the North Atlantic Caledonides: A regional view. *Geological Society Special Publication*, *335*(1), 767–793. https://doi.org/10.1144/SP335.31

Fossen, H., Cavalcante, G. C. G., Pinheiro, R. V. L., & Archanjo, C. J. (2018). Deformation—Progressive or multiphase? *Journal of Structural Geology*, *125*, 82–99. https://doi.org/10.1016/j.jsg.2018.05.006

Fossen, H., & Rykkelid, E. (1992). Postcollisional extension of the Caledonide orogen in Scandinavia: Structural expressions and tectonic significance. *Geology*, *20*(8), 737–740. https://doi.org/10.1130/0091-7613(1992)020<0737:PEOTCO>2.3.CO;2

Froitzheim, N., Pleuger, J., Roller, S., & Nagel, T. J. (2003). Exhumation of high- and ultrahigh-pressure metamorphic rocks by slab extraction. *Geology*, *31*(10), 925–928. https://doi.org/10.1130/G19748.1

Gee, D. G. (1975). A tectonic model for the central part of the Scandinavian Caledonides. *American Journal of Science*, *275-A*, 468–515.

Gee, D. G., Fossen, H., Henriksen, E., & Higgins, A. K. (2008). From the early Paleozoic platforms of Baltica and Laurentia to the Caledonide Orogen of Scandinavia and Greenland. *Episodes*, *31*(1), 44–51. https://doi.org/10.18814/epiiugs/2008/v31i1/007

Gee, D. G., Guezou, J.-C., Roberts, D., & Wolff, F. C. (1985). The central-southern part of the Scandinavian Caledonides. In D. G. Dee, & B. A. Sturt (Eds.), *The Caledonide Orogen—Scandinavia and related areas* (pp. 109–134). Chichester, UK: Wiley.

Gee, D. G., Janák, M., Majka, J., Robinson, P., & van Roermund, H. (2013). Subduction along and within the Baltoscandian margin during closing of the Iapetus Ocean and Baltica-Laurentia collision. *Lithosphere*, *5*(2), 169–178. https://doi.org/10.1130/L220.1

Gee, D. G., Klonowska, I., Andréasson, P.-G., & Stephens, M. B. (2020). Middle thrust sheets in the Caledonide orogen, Sweden: The outer margin of Baltica, the continent-ocean transition zone and late Cambrian-Ordovician subduction-accretion. In M. B. Stephens, & J. B.

Weihed (Eds.), *Sweden: Lithotectonic framework, tectonic evolution and mineral resources* (Vol. 50, pp. 517–548). London, England: Geological Society, London, Memoirs. https://doi.org/10.1144/M50-2018-73

Giorgis, D., Cosca, M., & Li, S. (2000). Distribution and significance of extraneous argon in UHP eclogite (Sulu terrain, China): Insight from in situ $^{40}Ar/^{39}Ar$ UV-laser ablation analysis. *Earth and Planetary Science Letters*, *181*(4), 605–615. https://doi.org/10.1016/S0012-821X(00)00221-1

Glodny, J., Ring, U., Kühn, A., Gleissner, P., & Franz, G. (2005). Crystallization and very rapid exhumation of the youngest Alpine eclogites (Tauern window, eastern Alps) from Rb/Sr mineral assemblage analysis. *Contributions to Mineralogy and Petrology*, *149*(6), 699–712. https://doi.org/10.1007/s00410-005-0676-5

Grimmer, J. C., Glodny, J., Drüppel, K., Greiling, R. O., & Kontny, A. (2015). Early- to mid-Silurian extrusion wedge tectonics in the central Scandinavian Caledonides. *Geology*, *43*(4), 347–350. https://doi.org/10.1130/G36433.1

Hacker, B. (2007). Ascent of the ultrahigh-pressure Western gneiss region, Norway. In M. Cloos, W. D. Carlson, M. C. Gilbert, J. G. Liou, & S. S. Sorenson (Eds.), *Convergent margin terranes and associated regions: A tribute to W. G. Ernst* (Vol. 419, pp. 171–184). Boulder, USA: Geological Society of America. https://doi.org/10.1130/2006.2419(09)

Hacker, B. R., Andersen, T. B., Johnston, S., Kylander-Clark, A. R. C., Peterman, E. M., Walsh, E. O., & Young, D. (2010). High-temperature deformation during continental-margin subduction & exhumation: The ultrahigh-pressure Western Gneiss Region of Norway. *Tectonophysics*, *480*(1–4), 149–171. https://doi.org/10.1016/j.tecto.2009.08.012

Hacker, B. R., & Gerya, T. V. (2013). Paradigms, new and old, for ultrahigh-pressure tectonism. *Tectonophysics*, *603*, 79–88. https://doi.org/10.1016/j.tecto.2013.05.026

Harrison, M. T., Célérier, J., Aikman, A. B., Hermann, J., & Heizler, M. T. (2009). Diffusion of ^{40}Ar in muscovite. *Geochimica et Cosmochimica Acta*, *73*(4), 1039–1051. https://doi.org/10.1016/j.gca.2008.09.038

Jakob, J., Andersen, T. B., & Kjøll, H. J. (2019). A review and reinterpretation of the architecture of the south and south-central Scandinavian Caledonides—A magma-poor to magma-rich transition and the significance of the reactivation of rift inherited structures. *Earth-Science Reviews*, *192*, 513–528. https://doi.org/10.1016/j.earscirev.2019.01.004

Janák, M., van Roermund, H., Majka, J., & Gee, D. (2013). UHP metamorphism recorded by kyanite-bearing eclogite in the Seve Nappe complex of northern Jämtland, Swedish Caledonides. *Gondwana Research*, *23*(3), 865–879. https://doi.org/10.1016/j.gr.2012.06.012

Janots, E., Brunet, F., Goffe, B., Poinssot, C., Burchard, M., & Cemic, L. (2007). Thermochemistry of monazite-(La) and dissakisite-(La): Implications for monazite and allanite stability in metapelites. *Contributions to Mineralogy and Petrology*, *154*(1), 1–14. https://doi.org/10.1007/s00410-006-0176-2

Kellett, D. A., Warren, C., Larson, K. P., Zwingmann, H., van Staal, C. R., & Rogers, N. (2016). Influence of deformation and fluids on Ar retention in white mica: Dating the Dover fault, Newfoundland Appalachians. *Lithos*, *254-255*, 1–17. https://doi.org/10.1016/j.lithos.2016.03.003

Kjøll, H. J., Andersen, T. B., Corfu, F., Labrousse, L., Tegner, C., Abdelmalak, M. M., & Planke, S. (2019). Timing of breakup and thermal evolution of a pre-Caledonian Neoproterozoic exhumed magma-rich rifted margin. *Tectonics*, *38*, 1843–1862. https://doi.org/10.1029/2018TC005375

Klonowska, I., Janák, M., Majka, J., Froitzheim, N., & Kośmińska, K. (2016). Eclogite and garnet pyroxenite from Stor Jougdan, Seve Nappe complex, Sweden: Implications for UHP metamorphism of allochthons in the Scandinavian Caledonides. *Journal of Metamorphic Geology*, *34*(2), 103–119. https://doi.org/10.1111/jmg.12173

Klonowska, I., Janák, M., Majka, J., Petrík, I., Froitzheim, N., Gee, D. G., & Sasinková, V. (2017). Microdiamond on Areskutan confirms regional UHP metamorphism in the Seve Nappe complex of the Scandinavian Caledonides. *Journal of Metamorphic Geology*, *35*(5), 541–564. https://doi.org/10.1111/jmg.12244

Klonowska, I., Majka, J., Janák, M., Gee, D. G., & Ladenberger, A. (2014). Pressure-temperature evolution of a kyanite-garnet pelitic gneiss from Areskutan: Evidence of ultra-high-pressure metamorphism of the Seve Nappe complex, west-Central Jamtland, Swedish Caledonides. In F. Corfu, D. Gasser, & D. M. Chew (Eds.), *New perspectives on the Caledonides of Scandinavia and related areas* (Vol. 390, pp. 321–336). London, UK: Geological Society of London. https://doi.org/10.1144/SP390.7 1

Kośmińska, K., Spear, F. S., Majka, J., Faehnrich, K., Manecki, M., Piepjohn, K., & Dallmann, W. K. (2020). Deciphering late Devonian-Early Carboniferous P-T-T path of mylonitised garnet-mica schists from Prins Karls Forland, Svalbard. *Journal of Metamorphic Geology*, 1–23. https://doi.org/10.1111/jmg.12529

Krabbendam, M., & Wain, A. (1997). Late-Caledonian structures, differential retrogression and structural position of (ultra)high-pressure rocks in the Nordfjord-Stadlandet area, Western gneiss region. *Norges Geologiske Undersøkelse Bulletin*, *432*, 127–139.

Kramar, N., Cosca, M. A., & Hunziker, J. C. (2001). Heterogeneous $^{40}Ar^*$ distributions in naturally deformed muscovite: In situ UV-laser ablation evidence for microstructurally controlled intragrain diffusion. *Earth and Planetary Science Letters*, *192*(3), 377–388. https://doi.org/10.1016/S0012-821X(01)00456-3

Kullerud, K. (1987). *Origin and tectonometamorphic evolution of the eclogites in the Tsäkkok Lens (Seve Nappes), Southern Norrbotten, Sweden (PhD Thesis)*. Oslo, Norway: University of Oslo.

Kullerud, K., Stephens, M. B., & Zachrisson, E. (1990). Pillow lavas as protoliths for eclogites: Evidence from a late Precambrian-Cambrian continental margin, Seve Nappes, Scandinavian Caledonides. *Contributions to Mineralogy and Petrology*, *105*(1), 1–10. https://doi.org/10.1007/BF00320962

Kylander-Clark, A. R. C., Hacker, B. R., & Mattinson, C. G. (2012). Size and exhumation rate of ultrahigh-pressure terranes linked to orogenic stage. *Earth and Planetary Science Letters*, *321-322*, 115–120. https://doi.org/10.1016/j.epsl.2011.12.036

Lanari, P., Vidal, O., De Andrade, V., Dubacq, B., Lewin, E., Grosch, E., & Schwartz, S. (2014). XMapTools: A MATLAB©-based program for electron microprobe X-ray image processing and geothermobarometry. *Computers & Geosciences*, *62*, 227–240. https://doi.org/10.1016/j.cageo.2013.08.010

Li, Z. H., Gerya, T. V., & Burg, J. P. (2010). Influence of tectonic overpressure on P-T paths of HP-UHP rocks in continental collision zones: Thermomechanical modelling. *Journal of Metamorphic Geology*, *28*(3), 227–247. https://doi.org/10.1111/j.1525-1314.2009.00864.x

Liao, J., Malusà, M. G., Zhao, L., Baldwin, S. L., Fitzgerald, P. G., & Gerya, T. (2018). Divergent plate motion drives rapid exhumation of (ultra)high pressure rocks. *Earth and Planetary Science Letters*, *491*, 67–80. https://doi.org/10.1016/j.epsl.2018.03.024

Liou, J. G., Tsujimori, T., Zhang, R. Y., Katayama, I., & Maruyama, S. (2004). Global UHP metamorphism and continental subduction/collision: The Himalayan model. *International Geology Review*, *46*(1), 1–27. https://doi.org/10.2747/0020-6814.46.1.1

Ludwig, K. R. (2012). *User's manual for isoplot 3.75, a Geochronological toolkit for Microsoft Excel*. Berkeley, California: Berkeley Geochronology Center Special Publication no. 5. Retrieved from http://www.bgc.org/isoplot_etc/isoplot.html

Majka, J., Be'eri-Shlevin, Y., Gee, D. G., Ladenberger, A., Claesson, S., Konečny, P., & Klonowska, I. (2012). Multiple monazite growth in the Åreskutan migmatite: Evidence for a polymetamorphic late Ordovician to late Silurian evolution in the Seve Nappe complex of west-central Jämtland, Sweden. *Journal of Geosciences*, *57*, 3–23. https://doi.org/10.3190/jgeosci.112

Majka, J., Rosén, Å., Janák, M., Froitzheim, N., Klonowska, I., Manecki, M., et al. (2014). Microdiamond discovered in the Seve Nappe (Scandinavian Caledonides) and its exhumation by the "vacuum-cleaner" mechanism. *Geology*, *42*(12), 1107–1110. https://doi.org/10.1130/G36108.1

McDonald, C. S., Regis, D., Warren, C. J., Kelley, S. P., & Sherlock, S. C. (2018). Recycling argon through metamorphic reactions: The record in symplectites. *Lithos*, *300-301*, 200–211. https://doi.org/10.1016/j.lithos.2017.11.028

Mørk, M. B. E., Kullerud, K., & Stabel, A. (1988). Sm-Nd dating of Seve eclogites, Norrbotten, Sweden—Evidence for early Caledonian (505 Ma) subduction. *Contributions to Mineralogy and Petrology*, *99*(3), 344–351. https://doi.org/10.1007/BF00375366

Mulch, A., & Cosca, M. A. (2004). Recrystallization or cooling ages: In situ UV-laser $^{40}Ar/^{39}Ar$ geochronology of muscovite in mylonitic rocks. *Journal of the Geological Society, London*, *161*(4), 573–582. https://doi.org/10.1144/0016-764903-110

Ohta, Y., Hiroi, Y., & Hirajima, T. (1983). Additional evidence of pre-Silurian high-pressure metamorphic rocks in Spitsbergen. *Polar Research*, *1*(2), 215–218. https://doi.org/10.1111/j.1751-8369.1983.tb00705.x

Parrish, R. R., Gough, S. J., Searle, M. P., & Waters, D. J. (2006). Plate velocity exhumation of ultrahigh-pressure eclogites in the Pakistan Himalaya. *Geology*, *34*(11), 989–992. https://doi.org/10.1130/G22796A.1

Pedersen, R.-B., Furnes, H., & Dunning, G. (1991). A U/Pb age for the Sulitjelma gabbro, North Norway: Further evidence for the development of a Caledonian marginal basin in Ashgill-Llandovery time. *Geological Journal*, *128*(2), 141–153. https://doi.org/10.1017/s0016756800018331

Petrík, I., Janák, M., Klonowska, I., Majka, J., Froitzheim, N., Yoshida, K., et al. (2019). Monazite behaviour during metamorphic evolution of a diamond-bearing gneiss: A case study from the Seve Nappe complex, Scandinavian Caledonides. *Journal of Petrology*, *60*, 1773–1796. https://doi.org/10.1093/petrology/egz051

Platt, J. P. (1993). Exhumation of high-pressure rocks: A review of concepts and processes. *Terra Nova*, *5*(2), 119–133. https://doi.org/10.1111/j.1365-3121.1993.tb00237.x

Ramsay, J. G. (1967). *Folding and fracturing of rocks*. New York, NY: McGraw-Hill.

Root, D., & Corfu, F. (2012). U-Pb geochronology of two discrete Ordovician high-pressure metamorphic events in the Seve Nappe complex, Scandinavian Caledonides. *Contributions to Mineralogy and Petrology*, *163*(5), 769–788. https://doi.org/10.1007/s00410-011-0698-0

Rosenberg, C. L., & Stünitz, H. (2003). Deformation and recrystallization of plagioclase along a temperature gradient: An example from the Bergell tonalite. *Journal of Structural Geology*, *25*(3), 389–408. https://doi.org/10.1016/S0191-8141(02)00036-6

Rubatto, D., & Hermann, J. (2001). Exhumation as fast as subduction? *Geology*, *29*(1), 3–6. https://doi.org/10.1130/0091-7613(2001)029<0003:EAFAS>2.0.CO;2

Rutter, E. H. (1976). The kinetics of rock deformation by pressure solution. *Philosophical Transactions of the Royal Society of London*, *283*(1312), 203–219. https://doi.org/10.1098/rsta.1976.0079

Rybacki, E., & Dresen, G. (2000). Dislocation and diffusion creep of synthetic anorthite aggregates. *Journal of Geophysical Research*, *105*, 17–26. https://doi.org/10.1029/2000JB900223

Sambridge, M. S., & Compston, W. (1994). Mixture modeling of multi-component data sets with application to ion-probe zircon ages. *Earth and Planetary Science Letters*, *128*(3-4), 373–390. https://doi.org/10.1016/0012-821X(94)90157-0

Santallier, D. S. (1988). Mineralogy and crystallization of the Seve eclogites in the Vuoggatjålme area, Swedish Caledonides of Norrbotten. *Geologiska Föreningen i Stockholm Förhandlingar*, *110*(2), 89–98. https://doi.org/10.1080/11035898809452646

Schneider, D. A., Faehnrich, K., Majka, J., & Manecki, M. (2019). $^{40}Ar/^{39}Ar$ geochronologic evidence of Eurekan deformation within the West Spitsbergen fold and Thrust Belt. In K. Piepjohn, J. V. Strauss, L. Reinhardt, & W. C. McClelland (Eds.), *Circum-Arctic structural events: Tectonic evolution of the Arctic margins and trans-Arctic links with adjacent orogens* (Vol. 541, pp. 153–168). Boulder, USA: Geological Society of America. https://doi.org/10.1130/2018.2541(08)

Smith, D. C. (1984). Coesite in clinopyroxene in the Caledonides and its implications for geodynamics. *Nature*, *310*(5979), 641–644. https://doi.org/10.1038/310641a0

Smye, A. J., Bickle, M. J., Holland, T. J. B., Parrish, R. R., & Condon, D. J. (2011). Rapid formation and exhumation of the youngest Alpine eclogites: A thermal conundrum to Barrovian metamorphism. *Earth and Planetary Science Letters*, *306*(3-4), 193–204. https://doi.org/10.1016/j.epsl.2011.03.037

Snilsberg, R. (1987). *Structural geology and metamorphic petrology of metasedimentary rocks in the Tsäkkok Lens (Seve Nappes) and in the Lower Köli volcanosedimentary rocks, Southern Norrbotten Caledonides, Sweden (PhD Thesis)*. Oslo, Norway: University of Oslo.

Spear, F. S. (2010). Monazite-allanite phase relations in metapelites. *Chemical Geology*, *279*(1-2), 55–62. https://doi.org/10.1016/j.chemgeo.2010.10.004

Stephens, M. B. (1977). Stratigraphy and relationship between folding, metamorphism and thrusting in the Tärna-Björkvattnet area, northern Swedish Caledonides. *Sveriges geologiska undersökning C*, *726*, 1–146.

Stephens, M. B. (1980). Occurrence, nature, and tectonic significance of volcanic and high-level intrusive rocks within the Swedish Caledonides. In D. R. Wones (Ed.), *The Caledonides in the USA* (pp. 289–298). Blacksburg, Virgina: Virginia Polytechnical institute and State University memoirs 2.

Stephens, M. B. (1982). Field relationships, petrochemistry and petrogenesis of the Stekenjokk volcanites, central Swedish Caledonides. *Sveriges geologiska undersökning C*, *786*, 1–111.

Stephens, M. B. (1988). The Scandinavian Caledonides: A complexity of collisions. *Geology Today*, *4*(1), 20–26. https://doi.org/10.1111/j.1365-2451.1988.tb00537.x

Stephens, M. B. (2020). Upper and uppermost thrust sheets in the Caledonide orogen, Sweden: Outboard oceanic and exotic continental terranes. In M. B. Stephens, & J. B. Weihed (Eds.), *Sweden: Lithotectonic framework, tectonic evolution and mineral resources* (Vol. 50, pp. 549–575). London, Memoirs: Geological Society. https://doi.org/10.1144/M50-2018-73

Stephens, M. B., Gustavson, M., Ramberg, I. B., & Zachrisson, E. (1985). The Caledonides of central-north Scandinavia—A tectonostratigraphic overview. In D. G. Dee, & B. A. Sturt (Eds.), *The Caledonide orogen—Scandinavia and related areas* (pp. 135–162). Chichester, UK: Wiley.

Stephens, M. B., & van Roermund, H. L. M. (1984). Occurrence of glaucophane and crossite in eclogites of the Seve nappes, southern Norrbotten Caledonides, Sweden. *Norsk Geologisk Tidsskrift*, *64*, 155–163.

Stølen, L. K. (1988). Tectonostratigraphy and structure of the Staloluokta area, Padjelanta, southern Norrbotten Caledonides, Sweden. *Geologiska Föreningen i Stockholm Förhandlingar*, *110*(4), 341–349. https://doi.org/10.1080/11035898809452669

Svenningsen, O. M. (2000). Thermal history of thrust sheets in an orogenic wedge: $^{40}Ar/^{39}Ar$ data from the polymetamorphic Seve Nappe complex, northern Swedish Caledonides. *Geological Magazine*, *137*(4), 437–446. https://doi.org/10.1017/S0016756800004210

Terry, T. P., Robinson, P., Hamilton, M. A., & Jercinovic, M. J. (2000). Monazite geochronology of UHP and HP metamorphism, deformation, and exhumation, Nordøyane, Western gneiss region, Norway. *American Mineralogist*, *85*(11-12), 1651–1664. https://doi.org/10.2138/am-2000-11-1208

Thelander, T. (2009). Bedrock map. In *The Caledonides in northern Sweden, scale 1:250 000. Southern part* (K222, pp. 1–51). Uppsala, Sweden: Sveriges Geolgiska Undersökning.

Uunk, B., Brouwer, F., ter Voorde, M., & Wijbrans, J. (2018). Understanding phengite argon closure using single grain fusion age distributions in the Cycladic Blueschist unit on Syros, Greece. *Earth and Planetary Science Letters*, *484*, 192–203. https://doi.org/10.1016/j.epsl.2017.12.031

van Roermund, H. L. M. (1985). Eclogites of the Seve Nappe, central Scandinavian Caledonides. In D. G. Dee, & B. A. Sturt (Eds.), *The Caledonide orogen—Scandinavia and related areas* (pp. 873–886). Chichester, UK: Wiley.

van Roermund, H. L. M. (1989). High-pressure ultramafic rocks from the Allochthonous Nappes of the Swedish Caledonides. In R. A. Gayer (Ed.), *The Caledonide geology of Scandinavia* (pp. 205–219). London, UK: Graham & Trotman. https://doi.org/10.1007/978-94-009-2549-6_17

Vernon, R. H. (1981). Optical microstructures of partly recrystallized calcite in some naturally deformed marbles. *Tectonophysics*, *78*(1-4), 601–612. https://doi.org/10.1016/0040-1951(81)90031-7

Warren, C. J. (2013). Exhumation of (ultra-)high-pressure terranes: Concepts and mechanisms. *Solid Earth*, *4*(1), 75–92. https://doi.org/10.5194/se-4-75-2013

Warren, C. J., Hanke, F., & Kelley, S. P. (2012). When can muscovite $^{40}Ar/^{39}Ar$ dating constrain the timing of metamorphic exhumation? *Chemical Geology*, *291*, 79–86. https://doi.org/10.1016/j.chemgeo.2011.09.017

Warren, C. J., Kelley, S. P., Sherlock, S. C., & McDonald, C. S. (2012). Metamorphic rocks seek meaningful cooling rate: Interpreting $^{40}Ar/^{39}Ar$ ages in an exhumed ultra-high pressure terrane. *Lithos*, *155*, 30–48. https://doi.org/10.1016/j.lithos.2012.08.011

Warren, C. J., Sherlock, S. C., & Kelley, S. P. (2011). Interpreting high-pressure phengite $^{40}Ar/^{39}Ar$ laserprobe ages: An example from Saih Hatat, NE Oman. *Contributions to Mineralogy and Petrology*, *161*(6), 991–1009. https://doi.org/10.1007/s00410-010-0576-1

Wintsch, R. P., & Yi, K. (2002). Dissolution and replacement creep: A significant deformation mechanism in mid-crustal rocks. *Journal of Structural Geology*, *24*(6-7), 1179–1193. https://doi.org/10.1016/S0191-8141(01)00100-6

Zachrisson, E. (1969). Caledonian geology of northern Jämtland-southern Västerbotten. *Sveriges geologiska undersökning C*, *644*, 1–33.

Zachrisson, E., & Stephens, M. B. (1984). Mega-structures within the Seve nappes, southern Norrbotten Caledonides, Sweden. In (Vol. 255, pp. 241–241). Stockholm, Sweden: Meddelanden från Stockholms Universitets Geologiska Institution.